INFORMATION TO USERS

This manuscript has been reproduced from the microfilm master. UMI films the text directly from the original or copy submitted. Thus, some thesis and dissertation copies are in typewriter face, while others may be from any type of computer printer.

The quality of this reproduction is dependent upon the quality of the copy submitted. Broken or indistinct print, colored or poor quality illustrations and photographs, print bleedthrough, substandard margins, and improper alignment can adversely affect reproduction.

In the unlikely event that the author did not send UMI a complete manuscript and there are missing pages, these will be noted. Also, if unauthorized copyright material had to be removed, a note will indicate the deletion.

Oversize materials (e.g., maps, drawings, charts) are reproduced by sectioning the original, beginning at the upper left-hand corner and continuing from left to right in equal sections with small overlaps. Each original is also photographed in one exposure and is included in reduced form at the back of the book.

Photographs included in the original manuscript have been reproduced xerographically in this copy. Higher quality 6" x 9" black and white photographic prints are available for any photographs or illustrations appearing in this copy for an additional charge. Contact UMI directly to order.

UMI

A Bell & Howell Information Company
300 North Zeeb Road, Ann Arbor MI 48106-1346 USA
313/761-4700 800/521-0600

EXPERIMENTAL CHARACTERIZATION OF A LOW DOSE-RATE AND A HIGH DOSE-RATE IRIDIUM-192 BRACHYTHERAPY SOURCE USING THE AAPM TG 43 DOSIMETRY PROTOCOL

Jean-Claude Anctil

Medical Physics Unit
McGill University, Montreal

September 1997

A thesis submitted to the Faculty of Graduate Studies and Research
in partial fulfilment of the requirements of the degree of
Master in Medical Radiation Physics

ABSTRACT

Current brachytherapy dosimetry protocols assume that a physical source may be approximated by a point source. A new brachytherapy dosimetry protocol, recently proposed by the American Association of Physicists in Medicine Task Group 43, has the advantage of using functions derived solely from measurements performed in the medium and uses a more realistic source geometry than the point source approximation. The aim of this work is to obtain the dosimetric functions required by this new protocol for both a low and a high dose-rate Iridium-192 brachytherapy source through dose measurements in a water-equivalent phantom.

Dose measurements have been performed using lithium fluoride thermoluminescent detectors positioned in a polystyrene phantom at distances from the source that vary from 1 cm to 10 cm, with 1-cm intervals, and at angles that vary from 0° to 170° with 10° intervals.

Our experimental results have clearly shown that the point-source approximation model can overestimate the dose to water, especially for the high dose-rate source, where we have found that differences between point-source estimates and exact measured values can differ by almost 30% for points along the longitudinal axis of the source.

RÉSUMÉ

Les protocoles actuels de dosimétrie de la curiethérapie utilisent l'approximation d'une source ponctuelle. Un nouveau protocole de dosimétrie applicable à la curiethérapie, proposé par le groupe de travail 43 de l'American Association of Physicists in Medicine, présente l'avantage d'utiliser des fonctions obtenues par des mesures effectuées entièrement dans un milieu comme l'eau, et, de plus, fait appel à une configuration géométrique plus réaliste des sources radioactives. La présente étude a été entreprise dans le but d'obtenir les fonctions dosimétriques du nouveau protocole associées à deux sources radioactives d'Iridium-192, soit une source de bas débit de dose et une source de haut débit de dose, et ce au moyen de mesures de dose dans un fantôme de matériel equivalent en eau.

Les mesures de dose ont été effectuées à l'aide de détecteurs thermoluminescents au fluorure de lithium placés dans un fantôme de polystyrène pour des distances variant de 1 à 10 cm, par intervalles de 1 cm, et pour une couverture angulaire variant de 0° à 170°, par intervalles de 10°.

Nos résultats expérimentaux ont clairement démontré qu'un protocole dosimétrique utilisant l'approximation ponctuelle de la source radioactive peut surestimer la dose à l'eau de près de 30% pour des points de calcul situés dans l'axe longitudinal d'une source à haut débit de dose.

ACKNOWLEDGEMENTS

I want to express my great gratitude to my supervisor, Dr Brenda G Clark, for her constant assistance throughout my research project. Her guidance has been of great help from the definition of the project to the completion of the thesis.

I would like also to thank Dr Clément Arsenault of the Dr. Léon Richard Oncology Centre for the many helpful discussions that greatly helped the progress of the experimental work.

I also thank Mr. Pierre Courteau for many helpful discussions and Mr. Clovis Leblanc for his dedicated work in building the polystyrene phantom.

TABLE OF CONTENTS

1.0 INTRODUCTION

Brachytherapy, which comes from the greek word *brachys* meaning "short", is the process of positioning one or more small sealed radioactive sources close to tumourous sites by interstitial, intracavitary or surface application. With this technique, a high dose can be given to a tumour while sparing normal tissues that surround the tumour because of the rapid dose fall-off with distance inherent with short source-tumour distances.

1.1 Brief Historical Review of Brachytherapy

The possibility of using radium to treat cancer was proposed soon after the discovery of radioactivity by Marie and Pierre Curie in 1898. In the early days of brachytherapy, the biological effect of radiation was not well known and treatments were empirically developed. For external applicators, physicians were using a standard dose called *skin erythema dose*, which was defined as that amount of x or γ radiation that just produced reddening of the human skin, as units of treatment to determine the quantity of radium expressed in terms of the number of milligram-hours required for a specific tumour size and location.

Advances in the capabilities to accurately quantify the radiation produced by radium sources lead to the development of the first dosage tables in the 1930s and 1940s (Paterson and Parker 1934, Quimby 1944). In these tables, the dose was expressed in a new unit, the *roentgen*, replacing the units of *skin erythema dose*. Radium sources were used for many years to treat cancer, but its use had several disadvantages. For example, radium had to be encapsulated, frequently with platinum, to prevent the leakage of the gaseous daughter product, radon, and the presence of relatively high energy photons placed constraints on the safe use and storage of radium sources.

In the 1950s, man-made radionuclides became available. A major advantage of the new sources were their lower mean photon energies which simplified radiation protection. Furthermore, the new sources produced a more concentrated energy deposition within the tumour volume. The most important radionuclides that have replaced radium and that are still in use today include cesium-137, iridium-192, iodine-125 and gold-198. All these radionuclides have a much shorter half-life than radium, which implies a larger specific

activity, thus making possible the construction of smaller, easier to insert sources. More recently, a number of new brachytherapy sources have been developed to optimize treatments (Nath 1993, Perera *et al.* 1994). They include americium-241, palladium-103, samarium 145 and ytterbium 169.

To reduce the exposure to medical personnel from brachytherapy sources, afterloading techniques, where sources are inserted into previously positioned applicators, have been introduced. Manual afterloading techniques were first used, and are still practiced today. However remote afterloading techniques have become more relevant because of the resulting elimination of radiation to personnel. Furthermore, remote afterloading techniques permit the use of sources that have an activity several thousand times larger than sources used in manual afterloading techniques, which enormously reduces the period of time the source is inserted into the patient. These new sources are called high dose-rate (HDR) sources, and a lot of effort has been devoted to improve understanding of the radio-biological impact of HDR treatments on both tumourous and normal tissue.

Brachytherapy treatment planning has also evolved over the years, from the early treatments which were based on the experience of the doctors, to current-day treatment planning systems (Pla 1989) that use computer programs to provide patients with the best possible treatment.

1.2 Changes in Dosimetry Protocols

Greater understanding of radiobiology combined with new technological developments have markedly improved the science of brachytherapy. Medical physicists have developed dosimetry protocols that have also become more accurate through the years. The current dosimetry protocol has adequately served the brachytherapy community for many years but a new dose calculation formalism has been recently proposed to account for the anisotropy of many new brachytherapy sources.

The current brachytherapy dosimetry protocol is based upon photon fluence around a point source in free space. Clinical applications require that we evaluate the dose distribution inside a patient, which implies non-point source configuration as well as attenuation and scattering of the radiation in tissue. While it is possible to determine a two-

dimensional dose distribution in a scattering medium from the knowledge of the two-dimensional distribution of photon fluence produced by a point source, actual brachytherapy sources are rarely spherical in structure and exhibit anisotropy due to self-attenuation of the radiation inside the source, limiting the use of the point-source approximation. The dose distribution produced in a scattering medium by an actual source can only be obtained through measurements in a water equivalent medium. In many treatments, the assumption that the radiation is isotropically produced around the source will lead to a negligible error. However in treatments such as a vaginal boost given by a high-dose rate Iridium-192 source, significant errors may be introduced by neglecting the anisotropy of the source.

For the dosimetry of interstitial brachytherapy sources, the American Association of Physicists in Medicine (AAPM) Task Group 43 (TG 43) has developed an improved dose calculation formalism (Nath *et al.* 1995). Under the new formalism, the exposure rate constant of a radionuclide, the apparent activity of the source, the exposure-to-dose conversion factor or the tissue attenuation factor of the old formalism are replaced by new functions directly derived from dose measurements in a water-equivalent phantom near the actual source. The new factors and functions include the dose rate constant, a radial dose function, an anisotropy function, a geometry factor, an anisotropy factor and the air kerma strength. These new functions vary with the actual source construction and geometry in addition to the primary photon spectrum and medium.

This research project was initiated to build a complete two-dimensional dose distribution data bank for both a low dose-rate and a high dose-rate Iridium-192 brachytherapy source. This data bank was then used to determine the functions defined by the new TG 43 protocol which can then be applied to provide improved treatment planning.

To obtain these data banks, a suitable water-equivalent phantom had first to be designed and constructed. Thermoluminescent detectors were selected to integrate the dose during the measurement process. Relevant analysis was performed to evaluate the dosimetry functions. A clinical case was also calculated using both the McGill treatment planning system and also the data bank obtained within this research project, and measurements were performed on a special phantom to assess and compare the accuracy of both protocols.

2.0 THE THEORY OF BRACHYTHERAPY DOSIMETRY

The dosimetry of brachytherapy uses basic laws of physics to evaluate the dose received by an organ during a treatment. This chapter shows the development of basic dosimetry concepts to obtain the equation used by the current brachytherapy dosimetry protocol implemented into most current commercial systems including the McGill Planning System (Pla 1989).

2.1 Basic Dosimetry Concepts

When a beam of ionizing radiation passes through material, photons interact with the medium in a two-stage process. The first step occurs when photons transfer part of their initial energy to electrons through collisions; this transfer of energy from the photons to the electrons is represented by a quantity called the kerma. The second step occurs when these high-speed electrons transfer their energy through a multitude of interactions with the electrons and atoms of the medium; this second transfer of energy is represented by the absorbed dose.

2.1.1 Definition of Kerma

The kerma, K, is defined as

$$K = \frac{d\varepsilon_{tr}}{dm} \qquad (2.1)$$

where $d\varepsilon_{tr}$ is the sum of the initial kinetic energies of all the charged ionizing particles liberated by uncharged particles (photons or neutrons) in a material of volume dv and mass dm. The units of kerma are joule per kilogram.

The term $d\varepsilon_{tr}$ includes not only the energy that charged particles lose through collisions but also the energy that these charged particles lose through radiation (bremsstrahlung). To account for the difference between the total energy released to material and the energy initially released to material but subsequently lost through radiative

processes, a new value, the collisional part of kerma, K_c, has been introduced and is expressed as

$$K_C = K(1-g) \qquad (2.2)$$

where g is the fraction of the electron energy lost to radiative processes.

It is useful to note that the same factor also relates μ_{ab}/ρ, the mass energy absorption coefficient to μ_{tr}/ρ, the mass energy transfer coefficient, that is

$$\frac{\mu_{ab}}{\rho} = \frac{\mu_{tr}}{\rho}(1-g) \qquad (2.3)$$

In brachytherapy dosimetry, because the mean photon energy is usually relatively small (< 1 MeV), it is assumed that very little energy will be lost through radiative process and therefore that g is much smaller than 1. Under these conditions, the collisional kerma is equal to the kerma.

The kerma rate, $\dot{K}$, is the increase of the kerma within a given time interval, dt, and is expressed as

$$\dot{K} = \frac{dK}{dt} \qquad (2.4)$$

The kerma rate units can be formed by any combination of a kerma unit and an appropriate time interval such as Gy h^{-1}.

The kerma in a small mass of medium is related to the kerma in air by

$$\frac{K_{med}}{K_{air}} = \frac{\left(\mu_{ab}/\rho\right)_{med}}{\left(\mu_{ab}/\rho\right)_{air}} \qquad (2.5)$$

or

$$K_{med} = K_{air}\left(\frac{\mu_{ab}}{\rho}\right)_{air}^{med} \qquad (2.6)$$

where $(\mu_{ab}/\rho)_{air}^{med}$ is the ratio of the mass energy transfer coefficient in the medium to that in air.

2.1.2 Definition of Dose

The absorbed dose, D, is defined in terms of the energy deposited by the radiation beam as it passes through the medium of interest. It is expressed as

$$D = \frac{d\varepsilon}{dm} \qquad (2.7)$$

where $d\varepsilon$ is the mean energy imparted by ionizing radiation to material of mass dm. The units of dose are the same as for the kerma that is joule per kilogram; a special name, the *gray*, symbol Gy, is associated to dose.

Similarly to the concept of kerma rate, we can define the dose rate, $\dot{D}$, as

$$\dot{D} = \frac{dD}{dt} \qquad (2.8)$$

Once again, the dose rate units can be formed by any combination of a dose unit and an appropriate time interval such as Gy h^{-1}.

In brachytherapy dosimetry, the conditions of charged particle equilibrium are assumed in the medium of interest. Then, the dose to medium equals the kerma in the medium, or

$$D_{med} = K_{air}\left(\frac{\mu_{ab}}{\rho}\right)_{air}^{med} \qquad (2.9)$$

or, in terms of the dose rate, we obtain

$$\dot{D}_{med} = \dot{K}_{air}\left(\frac{\mu_{ab}}{\rho}\right)_{air}^{med} \qquad (2.10)$$

2.2 Effect of Absorption and Scattering in the Medium

Equation 2.10 relates the kerma rate in air to the dose rate to a small mass of medium (that provides electronic equilibrium) in air. In brachytherapy, since the source is implanted in tissue, attenuation and scattering will take place between the source and the point of interest. To characterize the attenuation and scattering of radiation in a medium, a function, *T(d)*, has been defined as

$$T(d) = \frac{\dot{D}(d)_{med}}{\dot{D}(d)_{air}} \qquad (2.11)$$

where $\dot{D}(d)_{med}$ and $\dot{D}(d)_{air}$ are the dose rates in medium and to a small mass of medium in air, respectively.

Some authors have presented this function as a third order polynomial, for example Meisberger *et al.* (1968)

$$T(d) = 1 + Ad + Bd^2 + Cd^3 \qquad (2.12)$$

Kornelsen and Young (1981) illustrate the exponential absorption of the radiation and the increase of radiation due to scattering by representing this function as

$$T(d) = B_r e^{-\mu r} \qquad (2.13)$$

where

$$B_r = 1 + k_a(\mu r)^{k_b} \qquad (2.14)$$

and B_r is called a build-up factor, k_a and k_b are constants and μ is the linear attenuation coefficient in the medium.

2.3 Apparent Activity of a Source

Brachytherapy sources are usually calibrated in terms of air kerma rate at 1 meter. The strength of the source is often specified as apparent activity, A_{app}. It is defined as the activity of a point source of the same nuclide that produces the same air kerma rate at 1 meter as the source to be specified. The apparent activity is expressed in becquerel, Bq, where one Bq is equal to one disintegration per second. If a manufacturer specifies the strength of its source as apparent activity, the user must be careful to use the manufacturer's air kerma rate constant in dosimetric calculations.

2.4 The Air Kerma Rate Constant

The apparent activity of a radionuclide emitting photons is related to the air kerma rate by the air kerma rate constant, Γ_δ in the expression

$$\dot{K}_{air} = \frac{\Gamma_\delta A_{app}}{d^2} \qquad (2.15)$$

where Γ_δ is the air kerma rate constant, A_{app} is the apparent activity of the source and d is the distance between the source and the point of interest. Rearranging, the air kerma rate constant Γ_δ is given by

$$\Gamma_\delta = \frac{\dot{K}_{air} d^2}{A_{app}} \qquad (2.16)$$

The δ that appears as an index for the air kerma rate constant indicates that only photons with an energy above an arbitrary threshold are included in the definition of the air kerma rate.

The selection of the value δ depends on the application. In brachytherapy, the distances of interest range from about 1 cm to 10 cm from the source; therefore, it is not relevant to include in Γ_δ low-energy photons because such photons will not contribute to the absorbed dose at such distances. These low-energy photons are qualified as non-penetrating photons. Several authors (Glasgow and Dillman 1979, CFMRI 1982) suggest a photon energy lower limit that varies between 11 keV and 20 keV for Ir-192 sources.

To calculate the air kerma rate constant of a radionuclide we need to know with precision the disintegration scheme of the radionuclide. For example, if the disintegration scheme consists of an emission of photons of only one energy, we will have a photon energy fluence rate, $\dot{\Psi}$, (in J s^{-1} m^{-2}) at a distance r given by

$$\dot{\Psi} = \frac{NE}{4\pi r^2} \qquad (2.17)$$

where N is the number of photons emitted per second, E is the energy and r the distance from the source.

We also know that the kerma rate is related to photon energy fluence rate by

$$\dot{K} = \dot{\Psi}\left(\frac{\mu_{tr}}{\rho}\right) \qquad (2.18)$$

using 2.16 and 2.18, we then obtain

$$\Gamma_\delta = \frac{d^2}{A_{app}} \frac{NE}{4\pi r^2}\left(\frac{\mu_{tr}}{\rho}\right)_{air} \qquad (2.19)$$

(the units are Gy m^2 Bq^{-1} s^{-1})

If we consider a source of apparent activity equal to 1 Bq, at a distance of 1 m, the equation reduces to:

$$\Gamma_\delta = \frac{E}{4\pi}\left(\frac{\mu_{tr}}{\rho}\right)_{air} \qquad (2.20)$$

With E expressed in MeV, the equation becomes

$$\Gamma_\delta = \frac{1.6\times10^{-13} E}{4\pi}\left(\frac{\mu_{tr}}{\rho}\right)_{air} \qquad (2.21)$$

If the disintegration scheme includes several photons of various energies, we obtain the more general relation

$$\Gamma_\delta = \frac{1.6\times10^{-13}}{4\pi}\sum_{i=1}^{n} f_i E_i \left(\frac{\mu_{tr}(i)}{\rho}\right)_{air} \qquad (2.22)$$

where f_i is the number of photons emitted per disintegration with energy E_i.

For example, consider the disintegration of Ir-192, presented in table 2.1 (ICWG 1990, Johns and Cunningham 1983).

f_i (# of photons per disintegration)	E_i (MeV)	μ_{tr}/ρ (m^2 kg^{-1})
0.034	0.206	0.00268
0.291	0.296	0.00287
0.298	0.308	0.00287
0.831	0.317	0.00288
0.476	0.468	0.00296
0.032	0.485	0.00297
0.044	0.589	0.00296
0.081	0.604	0.00296
0.052	0.612	0.00296

Table 2.1: The most important transitions of the Iridium-192 radionuclide.

The application of equation 2.22 gives

$$\Gamma_\delta \approx 2.94\times10^{-17}\ \text{Gy m}^2\ \text{Bq}^{-1}\ \text{s}^{-1}$$

or

$$\Gamma_\delta \approx 106\ \mu\text{Gy m}^2\ \text{GBq}^{-1}\ \text{h}^{-1}$$

which is slightly less than the accepted value 113 μGy m^2 GBq^{-1} h^{-1} found in tables. The result approaches the tabulated value as more of the less significant transitions are included in the calculation.

2.5 Current Dosimetry Protocol

The combination of equations 2.10 and 2.15 leads to

$$\dot{D}_{med} = \frac{\Gamma_\delta A_{app}}{d^2}\left(\frac{\mu_{ab}}{\rho}\right)_{air}^{med} T(d) \qquad (2.23)$$

This expression represents the calculation most often used currently to evaluate the dose distribution produced by a given source arrangement.

It is well understood that the activity of a source decreases exponentially with time according to the relationship

$$A(t)=A_0 e^{-\lambda t} \qquad (2.24)$$

where A_0 is the initial activity of the source and λ is the decay constant of the radionuclide. The absorbed dose over a treatment period of time $\mathcal{T}$ will be obtained by using the time-dependent activity and integrating equation 2.23 over the time interval, $\mathcal{T}$.

If the period of treatment is short compared to the half life of the radionuclide, the integral will lead to

$$D_{med} = \frac{\Gamma_\delta A_{app}}{d^2}\left(\frac{\mu_{ab}}{\rho}\right)_{air}^{med} T(d)\cdot\mathcal{T} \qquad (2.25)$$

On the other hand, if the source decay cannot be neglected, we obtain

$$D_{med} = \frac{\Gamma_\delta A_{app}}{d^2}\left(\frac{\mu_{abs}}{\rho}\right)_{air}^{med} T(d)\frac{1}{\lambda}\left(1-e^{-\lambda\mathcal{T}}\right) \qquad (2.26)$$

For some elements with a long half-life like radium-226, cesium-137 or cobalt-60, equation 2.25 is always used. However for iridium-192 (low dose-rate source), iodine-125 or gold-198, the source decay cannot be neglected and equation 2.26 must be used to determine the duration of the treatment.

3.0 THE AAPM TASK GROUP 43 DOSIMETRY PROTOCOL

The previous chapter presented basic dosimetry concepts that lead the way to the current brachytherapy dosimetry protocol. This chapter presents in detail the dosimetric functions of this brachytherapy dosimetry protocol proposed in 1995.

3.1 General Formalism

The traditional method of calculating doses in a medium (eq. 2.23) has been used for many years. However it is always advantageous, and sometimes necessary, to determine doses *solely* from quantities measured in the medium. One option is to present the dose rate associated with a given source in a tabular form as a function of the position from the source. A more intuitive approach has been proposed within the TG 43 protocol (Nath *et al.* 1995) in which the effects of several physical factors on dose rate distribution are considered separately.

The dose rate at a point with coordinates (r,θ) from the center of a source of air kerma strength S_k can be expressed as

$$\dot{D}(r,\theta) = \Lambda S_k \frac{G(r,\theta)}{G(1,\pi/2)} F(r,\theta) g(r) \qquad (3.1)$$

where S_k is the air kerma strength (expressed in units of cGy cm^2 h^{-1} or U), Λ is the dose rate constant (cGy h^{-1} U^{-1} or cm^{-2}), $G(r,\theta)$ is the geometry factor (cm^{-2}), $F(r,\theta)$ is the anisotropy function (dimensionless) and $g(r)$ is the radial dose function (dimensionless). This relationship constitutes the basic equation of the new protocol. It is interesting to note that this formalism implies cylindrical symmetry of the source.

Each factor/function used by this protocol, with the exception of the geometry factor and the air kerma strength, must be determined through dose measurements in a water-equivalent phantom. The geometry factor is determined through simple arithmetic calculations, and the air kerma strength is measured with an ion chamber. The following sections will introduce each factor/function and present the equations required to determine these functions using only the dose measurements, the geometry factors and the air kerma strength.

3.2 Geometry factor, $G(r,\theta)$

The geometry factor, $G(r,\theta)$, accounts for the variation of relative dose due only to the spatial distribution of activity within the source, ignoring absorption and scattering in the source structure. It is defined as

$$G(r,\theta) = \frac{\int_V \left[\rho(\mathbf{r}')dV' / |\mathbf{r}' - \mathbf{r}|^2\right]}{\int_V \rho(\mathbf{r}')dV'} \qquad (3.2)$$

where $\rho(\mathbf{r}')$ represents the density of radioactivity (in MBq/cm^3 for example) at the point $\mathbf{r}' = (x', y', z')$ within the source. The origin of the vector $\mathbf{r}'$ can be arbitrarily set and can be outside the source. $\int_V$ denotes integration over the source core. dV' is a volume element located at $\mathbf{r}'$ in the source and $\mathbf{r}$ is the distance vector between the origin and the point of interest located outside the source.

As the three-dimensional distribution of $\rho(\mathbf{r})$ is uncertain for many sources, the point source or the line source approximation are used in practice for this particular function. The point source approximation can be used for spherical sources, such as Cs-137 brachytherapy sources. For a point source approximation, equation 3.2 reduces to

$$G(r,\theta) = \frac{1}{r^2} \qquad (3.3)$$

For a line source of length L, equation 3.2 reduces to

$$G(r,\theta) = \frac{\theta_2 - \theta_1}{Lh} \qquad (3.4)$$

or

$$G(r,\theta) = \frac{\theta_2 - \theta_1}{Lr\sin\theta} \qquad (3.5)$$

where the angles θ_1 and θ_2 are in radians and are illustrated in figure 3.1.

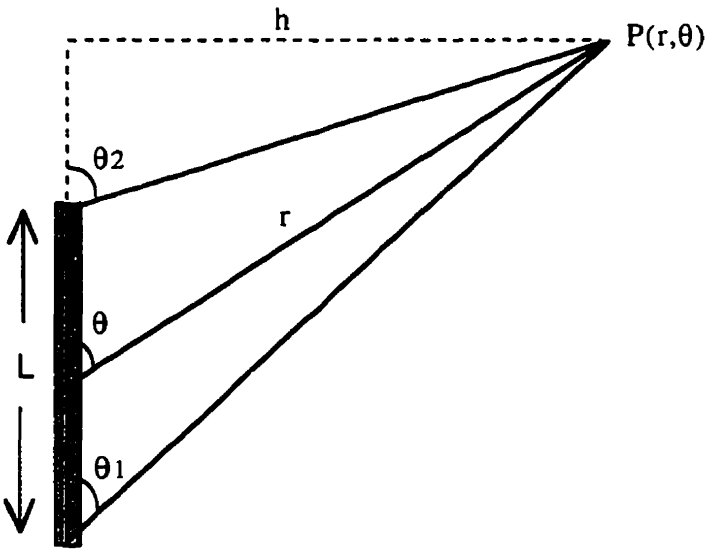

Figure 3.1 Geometry of a line source.

Equation 3.5 does not hold for on-axis points since, at these angles, both the numerator and the denominator equal zero. For on-axis points, the geometry factor reduces to

$$G(r,0^\circ)=\frac{4}{4r^2-L^2} \qquad (3.6)$$

For points on the transverse axis, we obtain

$$G(r,\pi/2)=\frac{2\tan^{-1}(L/2r)}{Lr} \qquad (3.7)$$

Equations 3.5 to 3.7 were used to build tables 3.1A and 3.1B that represent the geometry factors, $G(r,\theta)$, respectively for a 3-mm and 3.5-mm long brachytherapy source at various distances and angles. From these tables, the absence of variation with angular position at the higher distances indicates that the inverse square law (point-source approximation) is closely followed for these small sources.

Distance	0.5 cm	1.0 cm	2.0 cm	3.0 cm	4.0 cm	5.0 cm	10.0 cm
Angle							
0°	4.396	1.023	0.2514	0.1114	0.0626	0.0400	0.0100
10°	4.377	1.022	0.2514	0.1114	0.0626	0.0400	0.0100
20°	4.323	1.019	0.2512	0.1113	0.0626	0.0400	0.0100
30°	4.246	1.015	0.2509	0.1113	0.0626	0.0400	0.0100
40°	4.158	1.010	0.2506	0.1112	0.0625	0.0400	0.0100
50°	4.070	1.005	0.2503	0.1112	0.0625	0.0400	0.0100
60°	3.994	1.000	0.2500	0.1111	0.0625	0.0400	0.0100
70°	3.935	0.996	0.2498	0.1111	0.0625	0.0400	0.0100
80°	3.899	0.993	0.2496	0.1110	0.0625	0.0400	0.0100
90°	3.886	0.993	0.2495	0.1110	0.0625	0.0400	0.0100

Table 3.1A Values of the geometry factor, $G(r,\theta)$, in cm^{-2}, as a function of angular position and distance from the source for a brachytherapy source of length 3.0 mm.

Distance	0.5 cm	1.0 cm	2.0 cm	3.0 cm	4.0 cm	5.0 cm	10.0 cm
Angle							
0°	4.558	1.032	0.2519	0.1115	0.0626	0.0400	0.0100
10°	4.530	1.030	0.2519	0.1115	0.0626	0.0400	0.0100
20°	4.450	1.026	0.2516	0.1114	0.0626	0.0400	0.0100
30°	4.337	1.021	0.2513	0.1114	0.0626	0.0400	0.0100
40°	4.212	1.014	0.2509	0.1113	0.0625	0.0400	0.0100
50°	4.092	1.006	0.2504	0.1112	0.0625	0.0400	0.0100
60°	3.989	1.000	0.2500	0.1111	0.0625	0.0400	0.0100
70°	3.912	0.994	0.2497	0.1110	0.0625	0.0400	0.0100
80°	3.864	0.991	0.2494	0.1110	0.0625	0.0400	0.0100
90°	3.848	0.990	0.2494	0.1110	0.0625	0.0400	0.0100

Table 3.1B Values of the geometry factor, $G(r,\theta)$, in cm^{-2}, as a function of angular position and distance from the source for a brachytherapy source of length 3.5 mm.

3.3 Radial Dose Function, $g(r)$

The radial dose function, $g(r)$, accounts for the radial dependence of photon absorption and scatter in the medium along the transverse axis and is given by

$$g(r) = \frac{\dot{D}(r,\pi/2)}{\dot{D}(1,\pi/2)} \frac{G(1,\pi/2)}{G(r,\pi/2)} \qquad (3.8)$$

The geometry factor, $G(r,\theta)$, is factored out from the dose rates in defining $g(r)$. In other words, the inverse square law dependency of the dose does not affect $g(r)$. By definition, $g(r)$ equals 1 at $r = 1$ cm.

This function $g(r)$ is similar to the function $T(d)$ discussed in Section 2.2, in that they both represent the effect of absorption and scattering in the medium. The difference is that the new function is normalized at a distance $r_0 = 1$ cm; therefore we obtain

$$g(r) \approx \frac{T(d)}{T(d_0)} \qquad (3.9)$$

The accuracy of the approximation depends on differences in source construction between the source used for measurement and the source to which the data is to be applied.

3.4 Anisotropy Function, $F(r,\theta)$

The anisotropy function, $F(r,\theta)$, is a two-dimensional function that gives the angular variation of dose rate about the source with distance from the source due to self-filtration, oblique filtration of primary photons through the encapsulating material and scattering of photons in the medium. It is expressed as

$$F(r,\theta) = \frac{\dot{D}(r,\theta)}{\dot{D}(r,\pi/2)} \frac{G(r,\pi/2)}{G(r,\theta)} \qquad (3.10)$$

Once again, the geometry factor, $G(r,\theta)$, is factored out. By definition, $F(r,\pi/2) = 1$ for any values of r.

If the source were in vacuum, the anisotropy function would be independent of r. However, because of the scattering in the medium, the anisotropy function will become smoother as r increases.

3.5 Air Kerma Strength, S_k

The air kerma strength, or source strength, S_k, is defined as

$$S_k = \dot{K}_{air}(d) \cdot d^2 \qquad (3.11)$$

where d has to be large enough so that the source can be considered a point source. The value of S_k will therefore not change if we go from 1 m to 2 m, for example, since d^2 will increase by a factor of 4 but $\dot{K}_{air}$ will decrease by a similar factor. Correction for scattering and attenuation due to air have to be made. The units of the air kerma strength, S_k, are $\mu Gy\ m^2\ h^{-1}$ or $cGy\ cm^2\ h^{-1}$. A special unit, U, is used for the air kerma strength where $1\ U = 1\ cGy\ cm^2\ h^{-1}$.

The air kerma strength can be related to quantities defined in Chapter 2. Substituting for $\dot{K}_{air}$ from equation 2.15, equation 3.11 becomes

$$S_k = \Gamma_\delta A_{app} \qquad (3.12)$$

So the air kerma strength is equal to the apparent activity of a source multiplied by the air kerma rate constant of the radionuclide.

3.6 Dose Rate Constant, Λ

The dose rate constant, Λ, is defined as the dose rate per unit air kerma strength (U) at 1 cm along the transverse axis of the source, or

$$\Lambda = \frac{\dot{D}(1, \pi/2)}{S_k} \qquad (3.13)$$

The dose rate constant depends on the construction of the source. Two sources may have different dose rates at 1 cm but the same air kerma strength, S_k, because S_k is measured at a large distance from the source in order to fulfill the point source approximation. The units of Λ are cGy h^{-1} U^{-1} or cm^{-2}.

3.7 Anisotropy Factor, $\phi_{an}(r)$

If a large number of sources are randomly oriented, or if the degree of dose anisotropy around single sources is limited, the dose rate contribution to tissue from each source can be well approximated by the average radial dose rate as estimated by integrating the single anisotropy source with respect to solid angle. We then have

$$\dot{D}(r) = \frac{1}{4\pi}\int_0^{4\pi} \dot{D}(r,\theta)d\Omega \qquad (3.14)$$

where $d\Omega = 2\pi \sin\theta d\theta$ for a cylindrically symmetric dose distribution.

We can define an isotropy factor $\phi_{an}(r)$ as the ratio of the dose rate at distance r, averaged with respect to solid angle, to the dose rate on the transverse axis at the same distance. It is mathematically expressed as

$$\phi_{an}(r) = \frac{\dot{D}(r)}{\dot{D}(r,\pi/2)} \qquad (3.15)$$

Substituting for $\dot{D}(r)$ from equation 3.14, we obtain

$$\phi_{an}(r) = \frac{\int_{4\pi} \dot{D}(r,\theta)d\Omega}{4\pi \cdot \dot{D}(r,\pi/2)} \qquad (3.16)$$

or

$$\phi_{an}(r) = \frac{\int_0^{\pi} \dot{D}(r,\theta)\sin(\theta)d\theta}{2\dot{D}(r,\pi/2)} \qquad (3.17)$$

$\phi_{an}(r)$ is a factor slightly smaller than 1.0 because of the filtration of the source, usually minimal at $\theta = \pi/2$.

The anisotropy factor can be used to simplify equation 3.1. For points along the transverse axis at a distance r greater than $2L$, the equation for dose around a source using the point-source approximation (eq. 3.1) can be simplified to

$$\dot{D}(r,\pi/2) \approx \Lambda S_k \frac{r_0^2}{r^2} g(r) \qquad (3.18)$$

Eliminating $\dot{D}(r,\pi/2)$ from equations 3.15 and 3.18, the dose rate *at any angle*, at a distance r, can then be given by

$$\dot{D}(r) \approx \Lambda S_k \frac{r_0^2}{r^2} g(r)\phi_{an}(r) \qquad (3.19)$$

As seen in the previous equation, the use of the anisotropy factor adds a limited amount of anisotropy to the point-source model and reduces slightly the estimate of the dose rate $\dot{D}(r)$.

In practice, it is easier to work with an anisotropy factor that is not a function of the distance from the source. An average value $\overline{\phi}_{an}$ for various values of $\phi_{an}(r)$ can be defined as

$$\overline{\phi}_{an} = \frac{\sum \phi_{an}(r_i)/r_i^2}{\sum_i 1/r_i^2} \qquad (3.20)$$

where an inverse square law weighting factor has been introduced to account for the fact that sources closer to a given point make a larger contribution to the dose.

The concept of the anisotropy factor is used by treatment planning algorithms to incorporate some anisotropy of the source. Equation 3.1 can be approximated by

$$\dot{D}_{med}(r) = \Lambda S_k \frac{G(r,\pi/2)}{G(1,\pi/2)} g(r)\overline{\phi}_{an} \qquad (3.21)$$

Comparing equations 2.23 and 3.21, we see that the TG 43 protocol offers the option to add some numerical changes to the data bank of a standard treatment planning program to accomodate some aspects of the new formalism.

The various lookup tables used by standard treatment planning software can be modified by the input of new numerical values. Although many options exist to perform the transformations, the following substitutions were part of the recommendations of the TG 43 (Nath *et al.* 1995):

$$A_{app} \rightarrow S_k$$

$$\Gamma_\delta \left(\frac{\mu_{ab}}{\rho} \right)_{air}^{med} \rightarrow \frac{\Lambda \bar{\phi}_{an}}{G(1,\pi/2)}$$

$$T(r) \rightarrow r^2 G(r,\pi/2) g(r)$$

For example, the first substitution implies that the user must input the numerical value of the air kerma strength when the software requires the numerical value of the apparent activity of the source.

3.8 Concluding Remarks

The new formalism, as expressed in equation 3.1, contains many new functions. It is important to stress again that all these functions, with the exception of the geometry factor and the air kerma strength, are obtained through dose measurements in the medium. No assumptions are required concerning the disintegration scheme of the radionuclide. In principle, even the source strength would not be required. From the definition of the dose rate constant (equation 3.13), and since $F(1,\pi/2)$ and $g(1)$ both equal 1, equation 3.1 can also be represented as

$$\dot{D}(r,\theta) = \dot{D}(1,\pi/2) \frac{G(r,\theta)}{G(1,\pi/2)} \frac{F(r,\theta)}{F(1,\pi/2)} \frac{g(r)}{g(1)} \qquad (3.22)$$

When translated into words, equation 3.22 says that the dose rate at any position r, θ in the medium is equal to the dose rate at the point $r = 1cm$, $\theta = 90°$, multiplied by three factors that correct respectively for the distance from the source, the anisotropy of the source and the attenuation and scattering of the radiation within the medium at the point r, θ as compared to the point $r = 1cm$, $\theta = 90°$.

The next chapter will present the methodology required to measure the dose in a phantom to evaluate these new dosimetry functions.

4.0 EXPERIMENTAL DESIGN AND PROCEDURES

The design of the experimental work involved several aspects. From a consideration of the functions to be measured, we selected the most suitable detector for the application, determined the appropriate calibration technique that applies to our detectors, and designed a phantom that will reduce to a minimum any experimental uncertainties. This chapter describes these aspects of the experimental design.

4.1 Selection of Detectors

Stringent requirements are put on detector technology in brachytherapy dosimetry due to the presence of large dose gradients, a large range of dose rates and low photon energies, regularly encountered in measuring radiation produced by brachytherapy sources. Thus a suitable detector has to have a wide dynamic range, a flat energy response, a small size and a high sensitivity.

Because of the high cost and low sensitivity of radiochromic films (Muench *et al.* 1991) and problems of noise and low sensitivity of plastic scintillators (Perera *et al.* 1992), day-to-day brachytherapy dosimetry is almost entirely performed with the aid of silver-halide films, ionization chambers, silicon diodes and thermoluminescence detectors (TLDs). These are now discussed in detail.

4.1.1 Silver-halide Films

As a result of its large variation of responsivity as a function of the photon energy in the 50-300 keV region, silver-halide films are difficult to use for quantitative work in brachytherapy dosimetry. For Iridium-192 radiation propagating through water, many low-energy photons produced by Compton scattering will be strongly absorbed in the film emulsion because of the photoelectric effect; therefore the relation between optical density and dose becomes more unreliable. Furthermore, the use of films generally suffers from potential errors due to varying processing conditions, interfilm emulsion differences and artifacts caused by air pockets adjacent to the film. In spite of this, some authors (Podgorsak 1993a) have used silver-halide films to determine the anisotropy characteristics *in air* of a high dose-rate Iridium-192 source.

4.1.2 Ionization Chambers

The flat response of ionization chambers has always been recognized as a major asset for this family of detectors. However the relatively low sensitivity of ion chambers limits their usefulness in dosimetry of low-activity brachytherapy sources that produce a low dose rate even at distances as close as a few centimeters. More importantly, the requirement for a very small size detector is a second reason to discard this family of detectors, especially for cases where dose measurements have to be taken at distances equal or smaller than 1 cm. Since ion chambers have a relatively large collection volume, typically a minimum of 0.15 cm^3, doses are averaged over a large solid angle which can lead to erroneous dose gradient effects.

Furthermore, an uncertainty in the distance between a brachytherapy source and the point of collection of an ion chamber will give an error in the estimate of $\dot{D}(1, \pi/2)$. For example, an error of 300 μm in a separation distance of 1 cm results in a ~6% error in the dose rate estimate. Since it might be difficult to determine the distance between a brachytherapy source and the point of measurement of an ion chamber with a precision greater than 300 μm, this class of detectors should be avoided for measurements closer to the source than approximately 3 cm.

Ionization chambers have been used for measuring anisotropy functions at distances of 3 to 7 cm (Baltas *et al.* 1993, Zandona *et al.* 1995).

4.1.3 Silicon Diodes

The practical signal measured by a silicon diode can be orders of magnitude larger than the corresponding one measured with an ion chamber. Furthermore, since the collection volume of a silicon diode can be of the order of 2.5 mm in diameter and 60 μm in thickness, it is possible to know the distance between a brachytherapy source and the center of the collection volume of the diode with a precision greater than 100 μm. Meaningful measurements in the sub-centimeter distance range are therefore achievable with silicon diodes.

However, the response of a silicon diode is known to change as a function of the photon energy in the 50-300 keV region. Since the mean photon energy of the radiation produced by Ir-192 brachytherapy sources decreases as the distance from the source

increases (because lower-energy scattered photons accumulate at the same time as primary photons are attenuated), a distance-dependent correction factor has to be incorporated. This limits the use of silicon diodes in brachytherapy dosimetry. Some authors (Williamson *et al.* 1993, Kirov *et al.* 1995), have been able to use diodes in brachytherapy dosimetry by using Monte Carlo simulations to correct for energy response artefacts of silicon diodes.

4.1.4 Thermoluminescent Detectors

Thermoluminescent detectors are crystals whose structure allows absorption and emission of radiation in a well-understood manner as follows. In contrast to the structure of an atom, where electrons occupy discrete energy levels, interaction between atoms in a crystal lattice give rise to energy bands which can either be "allowed or "forbidden". Defects and impurities in the crystal provide energy levels in the forbidden band, creating metastable states for electrons (traps). When ionizing radiation is absorbed in a crystal, electrons are transfered from one allowed band (the valence band) to another allowed band of higher energy (the conduction band). Electrons (and holes thus created in the valence band) are free to move within the crystal. These free charge carriers then diffuse through the crystal until they reach traps in the crystal (figure 4.1). If an electron in a trap requires heat to get out of the trap and return to the ground state with the emission of light, the phenomenon is called thermoluminescence (Horowitz 1981). When a thermoluminescent crystal which has been exposed to radiation is heated, an increase in the rate of escape of trapped electrons will first occur, a maximum rate of escape will take place at some temperature followed by a decrease as the number of trapped electrons gradually go to zero.

The radiation emitted is proportional to the dose absorbed by the crystal. A plot of the light produced as a function of the temperature is called a glow curve. Since most phosphors contain a number of traps at various energy levels in the forbidden band, the glow curve consists of the superposition of a number of glow peaks at different temperature, as illustrated in figures 4.2a and 4.2b. The peaks correspond to different trapped energy levels; the peaks are numbered 1, 2, 3,...., the most important ones for dose measurements with LiF phosphors being peaks 3, 4 and 5.

The usefulness of a given phosphor trap for dosimetry depends on the temperature at which the glow peak takes place. Glow peaks that take place at temperatures lower than

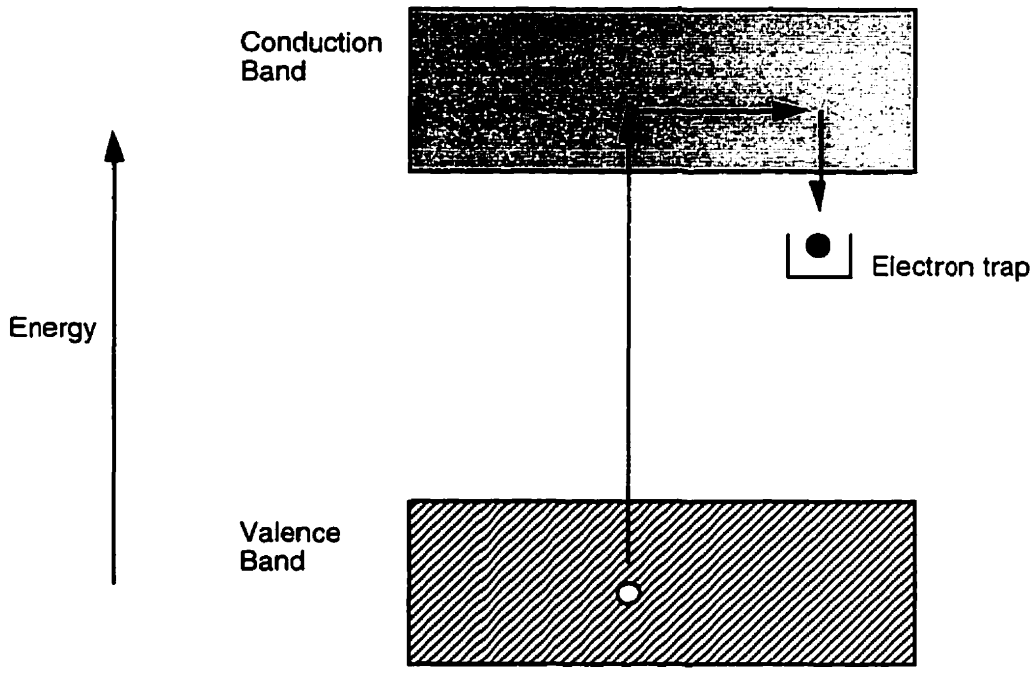

Figure 4.1 Electron energy-level diagram corresponding to the effect of radiation absorption by a thermoluminescent detector.

150° C correspond to the lower energy levels and have half-life of a few days at room temperature, which seriously limit their usefulness. Glow peaks that take place at temperatures around 200-225° C correspond to the more stable, higher energy levels and have half-life of months or years at room temperature, and are very suitable for dosimetry.

To obtain the accuracy required in radiation dosimetry, the dose stored in a TLD crystal is measured in a controlled environment using an instrument called a TLD reader. It is composed of a heater cup or planchette that is heated in a controlled fashion over a defined range of temperature from about 50°C to about 300°C. The emitted light is collected by a photomultiplier tube (PMT). An optical filter is usually used to filter out the infrared radiation from the thermal emission of the planchette in order to minimize signal not coming from the heated crystal. The signal is then recorded by a computer or any other counting or recording device.

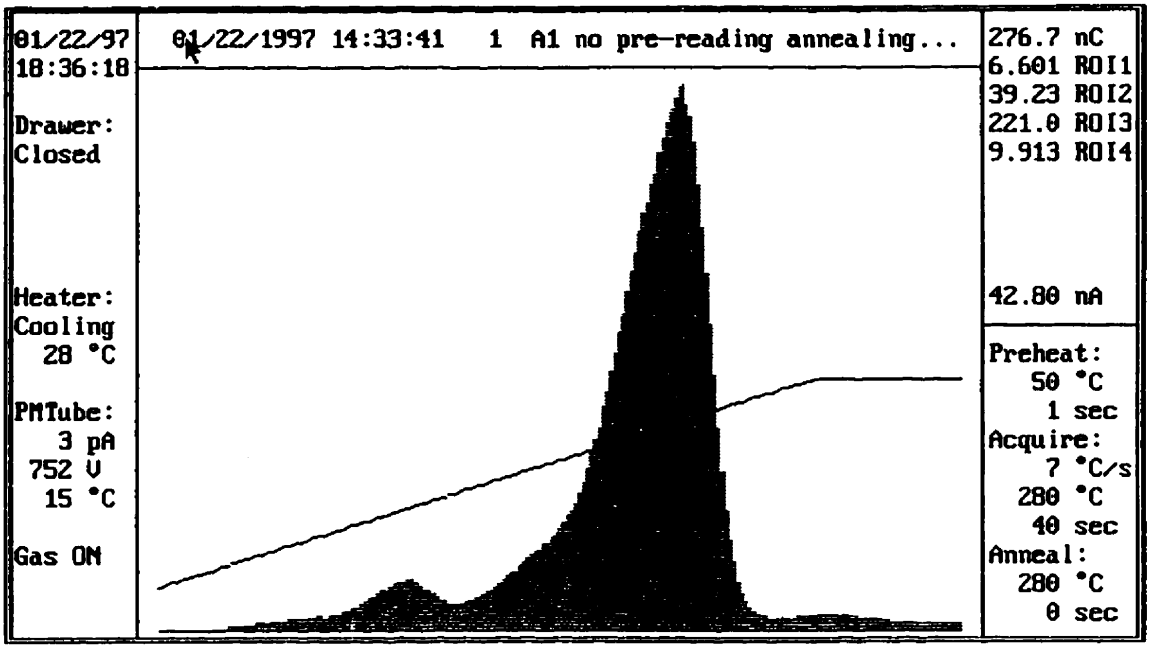

Figure 4.2a An experimentally obtained thermoluminescence glow curve.

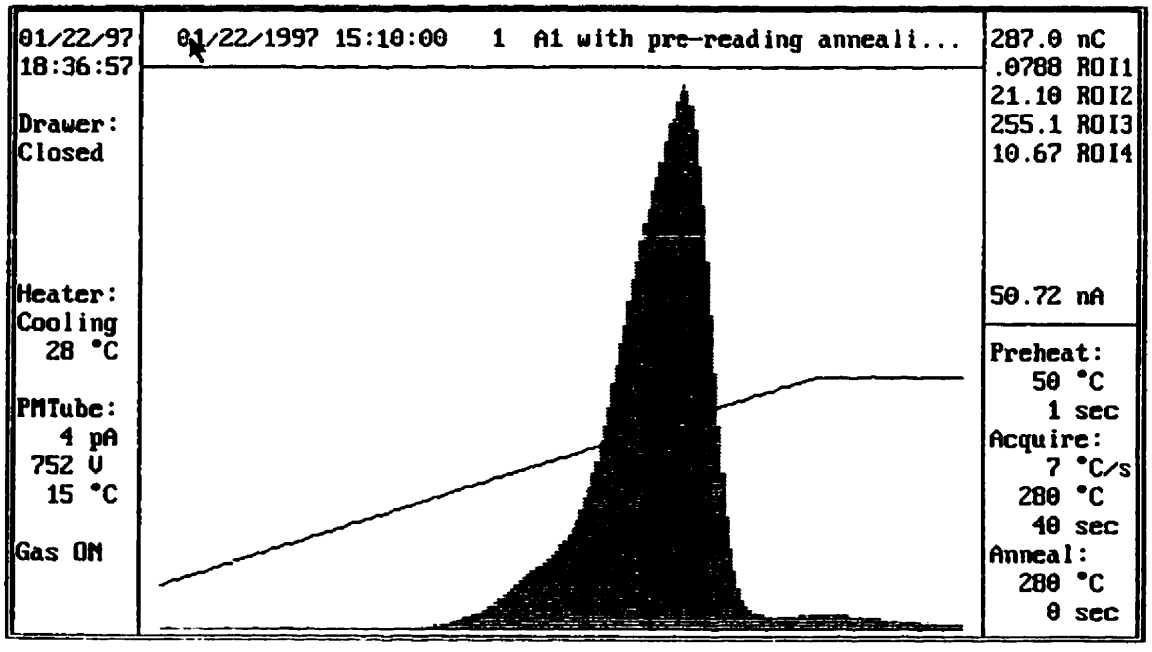

Figure 4.2b A thermoluminescence glow curve after the removal of peaks 1 and 2 through post-irradiation annealing.

There are many thermoluminescence phosphors available on the market but most measurements in radiotherapy are performed with lithium fluoride (LiF) because the effective atomic number of LiF is 8.2, which is close to the effective atomic number of soft tissue which is equal to 7.4. TLDs are manufactured as small rods, chips or powder. TLD rods and chips have to be carefully handled with tweezers since the grease from fingers may change the characteristics of the crystals. Improper handling can also lead to breakage of TLD rods and the response of a TLD would decrease proportionally to the reduction of the amount of active material. TLDs are reusable, they do not require cables since they are read after the irradiation period and they can be very small. However the dose information contained in a TLD is lost as the detector is heated during the reading phase, there is therefore no permanent record of the measured dose.

Since TLDs can be made very small, they can be positioned in small receptacles machined with great precision in a plastic phantom. Meaningful measurements down to the sub-centimeter distance range are therefore achievable with TLDs. Because of their small physical size, TLDs are often treated as point detectors. However, if TLDs are used in large dose gradient locations, the physical dimensions of the crystal cannot be neglected.

The sensitivity of TLDs is lower than an ion chamber. However, since the dose can be integrated over a long period of time, TLDs can be used in cases where very small dose rates exist. In practice, to save time, phantoms are usually designed in such a way that a large number of TLDs can be irradiated at the same time. In this way, absorbed doses at various positions can be concurrently measured.

TLDs must be calibrated before they are used for measuring an unknown dose. Since the response of the TLD material is affected by their previous radiation and thermal history, the material must be suitably annealed to remove residual effects. The standard pre-irradiation annealing procedure for LiF is 1 h of heating at 400°C and 24 h at 80°C (Cameron *et al.* 1968). The slow heating removes peaks 1 and 2 of the glow curve by decreasing the trapping efficiency. Peaks 1 and 2 can also be eliminated by postirradiation annealing for 10 min at 100°C. By removing these peaks through annealing, the glow curve becomes more stable and therefore predictable. Figure 4.2b showed an example of a glow curve after the removal of peaks 1 and 2 through post-irradiation annealing.

The dose response curve for TLDs is generally linear up to approximately 10 Gy but beyond that, there is a supralinear region, followed by a saturation region and, at very

high absorbed doses, a decrease of the emitted light signal. The minimum detectable dose can be as low as 10 μGy.

4.1.5 Concluding Remarks

From consideration of the task to be performed within this research project, thermoluminescent detectors were chosen as the detector offering the best compromise between small size, sensitivity, energy response and ease of acurate positioning. LiF TLD-100 rods manufactured by Solon/Harshaw (Solon Technologies, Inc., Solon, OH, USA) were selected. These TLD rods are 1 x 1 x 6 mm^3 in size and they can easily be handled with tweezers.

A difficulty in estimating absorbed dose to water from TLD readings in a given experiment is the determination of some correction factors. The main factors that apply for this research project are the variation of sensitivity with photon energy, the volume averaging effect and the inter-detector effect, which are discussed in Section 4.4.

4.2 Design of the phantom

Having selected our detectors, the most important task was to design and build a phantom that would provide us with the most convenient procedure and the most reliable experimental results.

4.2.1 Material of the Phantom

To comply with the TG 43 brachytherapy dosimetry protocol, we need to perform measurements in water or in a water-equivalent phantom. Since we wanted to use TLDs, a solid phantom was our only choice. Furthermore, as mentioned above, measurements of parameters associated with the dosimetry of brachytherapy sources require accurate source-to-detector distances. A solid phantom has a definite advantage since it can be precisely machined to accomodate sources, and distances can be accurately known. However radiation characteristics of various solid materials can differ from the radiation characteristics of water, making the selection of a solid phantom material a variable having an important effect on the accuracy of the experimental results.

The most important transitions of the photon spectrum of Iridium-192, which are in the range of 205 to 615 keV, were shown in table 2.1. For these photons, Compton scattering is the dominant interaction, indicating that the difference in electron density of various materials will play a key role in the dosimetric characteristics of the materials. Meli *et al.* (1988) have clearly shown, through depth-dose measurements, that polystyrene and solid water, which have densities close to that of water, are suitable phantom materials even in the absence of full scatter conditions.

In consideration of the restraints imposed by cost and material availability, our phantom was build with polystyrene.

4.2.2 Description of the Phantom

The position of the source relative to the thermoluminescent detectors are shown in figure 4.3. The TLD receptacles are 1.5 mm in diameter and 6 mm deep in order to hold detectors of dimension 1 mm x 1 mm x 6 mm. There are TLD receptacles at distances of 1 cm to 10 cm, at every centimeter, and at angles that vary between 0° and 170°, at every 10 degrees, except for the shorter distances where the 150°, 160° and 170° positions are not always available due to the presence of the applicator.

The Ir-192 source is positioned inside an endobronchial applicator which is centered at a depth of 3 mm inside the phantom. A groove was machined into the phantom to position the applicator. A cover strip tightly holds the applicator in place.

While it is possible to perforate hundred of holes in a single piece of plastic and then fill some of them with TLDs to make measurements, the numerous air gaps that are then present during the measurement process can introduce erroneous results. Polystyrene plugs can be used to fill holes that are not filled with TLDs at a given time, but this is not very practical.

To reduce to a minimum the effect that the close presence of an air gap or another detector could produce on a given reading, the pathway between the source and a given TLD should ideally be unobstructed every time a set of measurements is taken. In other words, each set of measurements should be performed at all angles at the same time but for

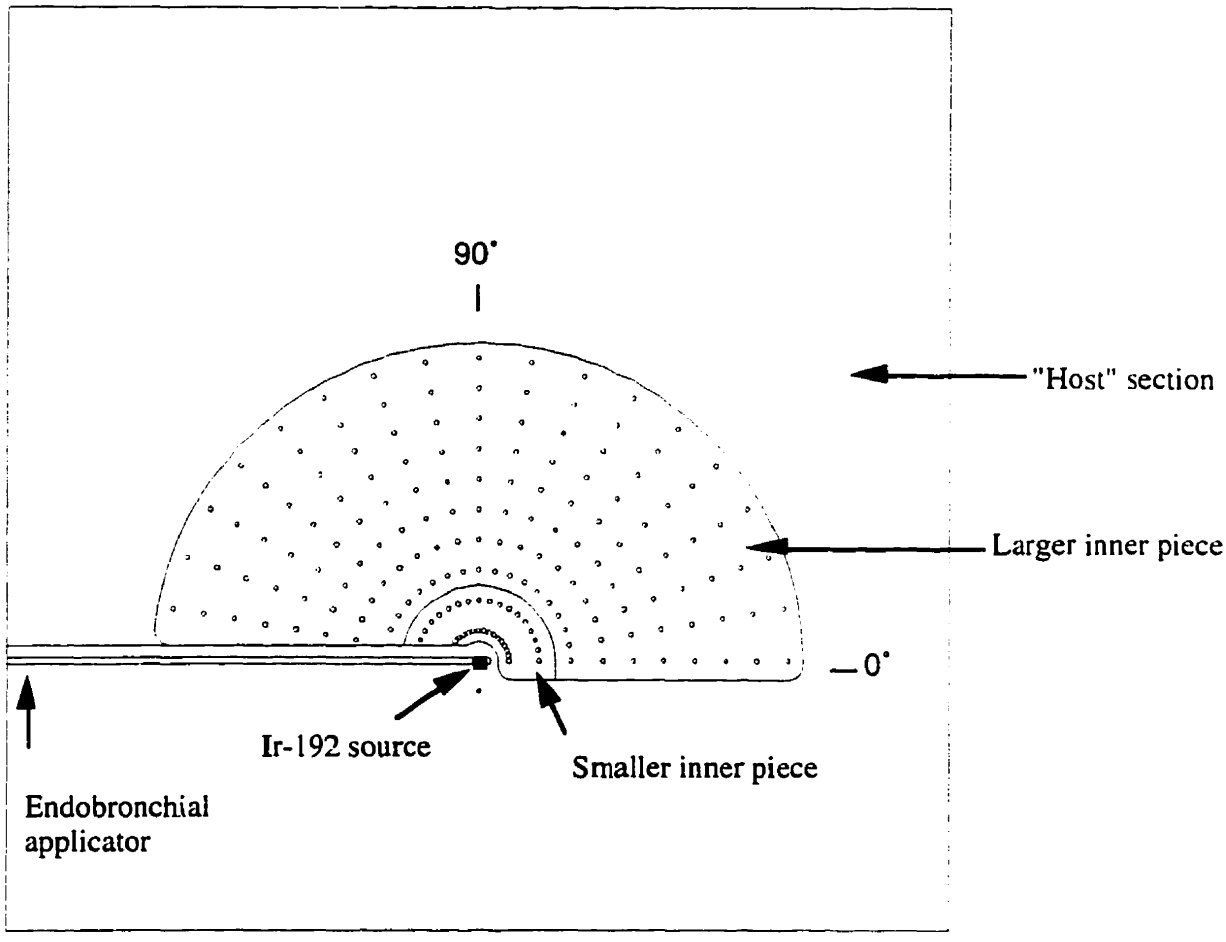

Figure 4.3 Drawing of the polystyrene phantom.

a single distance. The easiest way to achieve this is to machine ten different inner pieces, all of the same size, each one having holes at all angles but at distances that vary between 1 cm and 10 cm. To economise on material, the inner pieces were machined into two different dimensions: smaller inner pieces that can be either blank or perforated at a distance of 1 cm or 2 cm, and larger inner pieces that can also be blank or perforated at distances of 3 cm to 10 cm. A minimum of three smaller inner pieces and eight larger ones were then required. In practice, it was realized that to have 1.5-mm holes at every 10 degrees at a distance of 1 cm from the source was not appropriate. There was just not enough material around each hole to obtain reliable results. It was then decided that at both distances of 1 cm and 2 cm, two inner pieces would be machined; one piece perforated at 0°, 20°, 40°, 60°,..., and the other piece perforated at 10°, 30°, 50°, 70°,.... This design provided more

scattering medium around each TLD rod. A total of five inner pieces and eight larger ones were then machined.

Figure 4.4 is a photograph of our phantom. The phantom (called the *puzzle phantom*) is made of several pieces of polystyrene. The biggest block of polystyrene is the "host" section of the phantom. Its dimensions are 30 cm x 30 cm x 2.5 cm. There are three holes in the block of polystyrene which are used to remove the tightly fitting inner pieces from the host block using a small metal tool to push from the rear. Figure 4.4 shows the host block, the smaller blank piece, the two small pieces perforated at a distance of 1 cm from the source, the two small pieces perforated at a distance of 2 cm from the source and four of the eight larger inner pieces perforated at 3, 8, 9 and 10 cm respectively.

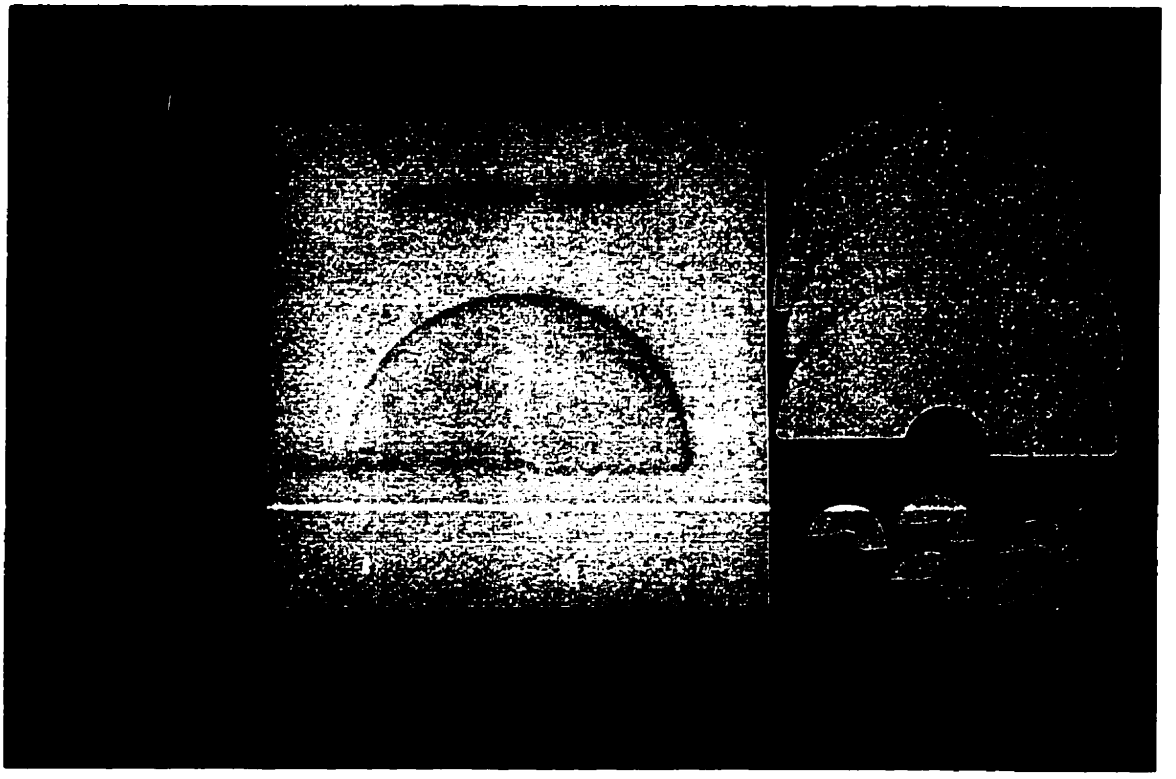

Figure 4.4 Photograph of the polystyrene phantom.

Since the definition of the radial dose function and the dose rate constant relies on the measurement of the dose rate at 1 cm, an error of 50 μm or less in the source-to-TLD rod distance would be required to give an uncertainty of less than one percent due to

positioning alone. Such a precision is difficult to achieve because the source is inserted through an endobronchial catheter fixed into a slot into the phantom. The sources are slightly smaller than the catheter and it is impossible to know the exact transverse position of the source inside the catheter, especially with the low dose-rate Ir-192 source which is more than half a millimeter smaller than the interior diameter of the catheter. To solve this problem, a hole was drilled exactly 2 cm below the TLD rod positioned at 1cm,+90°. Therefore by taking the average of the two TLD rods placed at 1 cm from the source, respectively at angular positions +90° and -90°, the distance error in the estimate of $\dot{D}(1,\pi/2)$ was minimized.

Several authors have studied, either experimentally or through Monte Carlo calculations, the radial dependence of photon absorption and scatter in a medium (Thomason and Higgins 1989, Weaver *et al.* 1989, Nath *et al.* 1990, Williamson 1991). In some cases, a comparison between the published results demonstrate a difference greater than that explained by experimental error. One possible explanation is that the size of the phantom can somewhat affect the experimental results.

Some authors (Sakelliou *et al.* 1992) have determined the effect of the size of the phantom on the radial dose function through Monte Carlo calculations. As is well known, the Compton scattering differential cross section is forward peaked at high photon energies but it is more isotropic at lower energies. Their study shows, for instance, that for spherical phantoms of 15 cm and 20 cm radius respectively, the radial dose function will not be very different up to a distance from the Ir-192 source of 8 cm, but then at 10 and 12 cm, a smaller radial dose function will be obtained with the smaller phantom because of reduced scattering. An even bigger difference will be noticed at a radius of 15 cm because for the case of the smaller phantom there will be no room for backscattering, leading to a much smaller dose.

On the other hand, some other authors (Serago *et al.* 1991) have studied several clinical applications where iridium sources may be anatomically located so that the full scattering requirement is not satisfied. Such clinical cases include treatment of breasts, head and neck, endobronchial and esophageal tumours. Experimental results have indicated that although dose reductions of the order of 8% can be expected at an interface, minimal dose reduction was found within the volume of the implant itself, even for source-to-air interface distances as small as 1 cm.

When experimental data was taken with our phantom, the Ir-192 source and the TLDs were placed into receptacles at a shallow depth of the 30 cm x 30 cm x 2.5 cm host section of the polystyrene phantom. Additional polystyrene slabs were placed above and below the machined slab to create a 30 cm x 30 cm x 16.5 cm scattering volume. This resulted in a minimum source-to-phantom-surface distance of 8 cm with all TLD chips at least 5 cm (and most of them at more that 8 cm) from the closest boundary of the phantom. For an experiment of this kind, a compromise has to be made on the size of the phantom. Our phantom is of comparable size to the one used by other scientists (Kirov *et al.* 1995) and is of an appropriate size to correctly characterize the dosimetry functions associated with our Ir-192 sources.

4.3 Accurate use of TLD Detectors

4.3.1 General Description of the TLD reader

The TLDs used in this research project were read and analysed using a commercially available system (Harshaw System 3500 TLD Reader, Harshaw/Bicron, Solon, Ohio, USA). The Harshaw System 3500 TLD Reader is a PC-driven instrument for thermoluminescence dosimetry measurement. The unit reads one dosimeter per loading. The software provides real-time monitoring of the instrument's operating conditions and display of the glow curves and response values. The reader uses contact heating of the planchette that produces reproducible temperature ramps. To improve the accuracy of low-exposure readings, the reader provides for nitrogen to flow around the planchette during the heating cycle. The nitrogen flow eliminates the unwanted oxygen-induced TL signals (Meigooni *et al.* 1995).

For accurate annealing of the TLDs a specially designed oven is also used. This oven (PTW, TLDO Model, PTW-Freiburg, Freiburg, Germany) is controlled by a programmable microprocessor. Two pre-programmed heating cycles are available. The risk of errors arising from non-reproducible annealing is reduced by the use of two pre-programmed annealing cycles, a first program for the annealing of TLDs before irradiation, and a second program for preheating the detectors after irradiation and before reading.

4.3.2 Reading Protocol

The various acquisition parameters, for example, the time temperature profile (TTP) are first defined. The TTP selected for this project consists of a data acquisition ramp of 7°C s^{-1} that starts at 50°C and goes to 280°C, followed by a flat temperature phase at 280°C for an additional 7 seconds. Once the acquisition parameters were properly set, the TLDs were put on the heating planchette, one at a time, to be read. Figure 4.2 shows a typical glow curve. Since we performed preread anneal, peaks 1 and 2 of the glow curve do not appear in figure 4.2. The glow curve was then formed by the superposition of peaks 3, 4 and 5 and the presence of some infra-red background at the end of the curve. We see that for this particular example the total charge is 287 nC.

The dose corresponding to the glow curve of figure 4.2 is about 16 cGy. We see that at this dose level, the glow curve seems relatively free from background noise. For the measurement of much smaller doses, the infrared background can be important. A computerized glow curve deconvolution routine is then used to separate a total glow curve into its background components and individual glow peaks. Using this special routine, it has been possible to measure doses as low as 0.09 cGy.

In conclusion, proper use of the Harshaw model 3500 TLD reader, the accessory oven and the deconvolution routine gave reliable results. Any dose larger than about 0.5 cGy could be accurately measured. The methodology was then established to characterize both a high dose-rate and a low dose-rate Ir-192 brachytherapy source.

4.3.3 Calibration and Energy Response of the TLDs

Thermoluminescence detectors are relative detectors. When a TLD detector is read, a total charge, in nC, is measured by the photomultiplier tube. A calibration factor, expressed in nC cGy^{-1}, is required to determine the dose integrated by the TLD. To obtain this calibration factor, each TLD is irradiated using a calibrated photon beam, in this work the one produced by a 6 MV linear accelerator. Furthermore, since the sensitivity of LiF TLDs vary as a function of the photon mean energy, a calibration factor has also to be found to account for the TLD change of sensitivity. In addition, some special phantom geometry can induce experimental artefacts. For instance, some TLDs can be positioned very close to other ones and the radiation can be erronously masked or scattered. This

section will address all the aspects of TLD calibration as applied to our measurement geometry.

4.3.3.1 TLD Annealing Cycles

To obtain accurate and precise results with TLDs, a strict procedure has to be established and rigourously followed. The most important aspect in the good use of TLDs is related to their heating cycles.

Several authors have suggested differing annealing techniques. For some authors (Cameron *et al.* 1964) the annealing procedure consists of a 400°C annealing for 1 h, followed by a 80°C annealing for 24 h, before irradiation. The purpose of 400 °C treatment is complete de-excitation of all traps in the phosphor, and the 24 h annealing at 80 °C reduces the contribution of peaks 1-3 to ~ 1.5% of the total thermoluminescence (Horowitz 1981). Other authors (Booth *et al.* 1972) have proposed a different annealing technique known as postirradiation or prereadout annealing with heating the TLDs at 400°C for 1 h before irradiation and then 10-15 minutes of heating at 100°C before the readout. The latter technique has the advantage of reducing the time required to anneal the TLDs; similar results were obtained with both annealing cycles (Dhar *et al.* 1973).

The annealing procedure suggested by the manufacturer of the LiF TLD-100 rods includes a preirradiation heating phase as well as a post-irradiation heating phase. Before the irradiation, the manufacturer suggests first a heating phase of the TLDs at 400°C for 1 h, followed by a cooling phase of the TLDs to 100°C, and a stable phase at 100°C for 2 h and then a final cooling phase of the TLDs to ambient temperature. After the irradiation, the manufacturer suggests heating the TLDs at 100°C for 10 minutes and then cooling the TLDs to ambient temperature. These two heating cycles are the two heating cycles that are pre-programmed in the accessory oven that was used in this project. After investigating several options, we determined that these two heating cycles were suitable for our work. Kron *et al.* (1993) also used these annealing cycles and obtained very good results.

4.3.3.2 Preliminary Irradiation with a 6-MV photon beam

Seventy-five TLD rods were available for this study. The TLDs were first irradiated with a 6 MV photon beam to assess the stability in the energy response of individual detectors and to determine the precision that can be obtained with TLDs. To

obtain maximum dose uniformity among the TLDs, the crystals were positioned at a depth of 10 cm, where the beam profile is very flat. To evaluate the stability of the individual and the group average charge as a function of time, a dose of 100 cGy were given to the rods in a series of 13 exposures.

Table 4.1 presents the results obtained on a group of 25 TLD rods. We see that the response of the TLDs started at a value of 19.4 nC/cGy but the average sensitivity has dropped by about 5% after the eighth irradiation. The subsequent five irradiations produced a reduction in the response of the TLDs of less than 1%. We concluded that the TLDs had reached a point of relative equilibrium (although this calibration factor was checked at regular intervals throughout this study). This table also demonstrates the variation in individual sensitivity of TLD crystals, illustrating the requirement for individual calibration factors.

The precision of the dose measurement with the TLDs is calculated from the reproducibility of the dose reading of the individual crystals. The precision of dose measurement (Kron *et al.* 1993) is expressed as 2 standard deviations given as percentage of the average measured dose of the last six irradiations, which are tests # 8 to 13 in table 4.1. We see that seven TLD rods present an error equal or higher than 3% whereas the remainer have stability of less than 3%. These seven TLD rods were discarded, and we consider that the precision of the individual TLD rods used in this study is equal or better than 3%.

A similar analysis was also performed on the remaining 50 TLD rods.

4.3.3.3 Calibration with a 6-MV photon beam

The first series of measurements was aimed at characterizing a low dose-rate Ir-192 brachytherapy source. It was impractical to measure doses larger than approximately 7 cGy due to the length of irradiation time required. It was decided that a total dose of about 7 cGy would be appropriate. Eventhough TLDs are said to have a linear response from a few cGy to more than 100 cGy, some authors (Meigooni *et al.* 1995) have demonstrated that there is a small amount of supralinearity in TLDs at all doses, therefore the TLDs were calibrated at the linac at a dose of about 7 cGy. To give a dose of only 7 cGy at 10 cm deep in a polystyrene phantom relates to only 10 Monitor Units (MUs) on the linac. To

TLD	Total Charge (nC)																
	Test 1	Test 2	Test 3	Test 4	Test 5	Test 6	Test 7	Test 8	Test 9	Test 10	Test 11	Test 12	Test 13	Average (Test 8 to 13)	Standard Deviation σ	(100 x σ)/ average	error in %
A1	2152	2136	2094	2090	2100	2017	2062	2029	2003	1973	2051	2060	2026	2024	32.0	1.6	3.2
A2	2108	2078	2061	2050	2063	2040	2055	1999	1994	1989	1994	1938	1941	1976	28.3	1.4	2.9
A3	2100	2140	2109	2097	2129	2073	2092	2071	2048	2044	2042	2056	2025	2048	15.3	0.7	1.5
A4	2119	2105	2097	2089	2114	2096	2039	2011	2042	2046	2019	2036	2036	2032	13.7	0.7	1.3
A5	2022	2039	2039	2031	2013	2011	2016	1958	1951	1954	1945	1958	1963	1955	6.3	0.3	0.6
B1	2013	1991	1983	1996	1995	1962	1941	1926	1902	1916	1919	1902	1887	1909	14.3	0.7	1.5
B2	684	720	714	711	716	709	672	691	656	661	657	651	650	661	15.2	2.3	4.6
B3	1970	2029	2006	1984	2006	1982	1988	1942	1910	1934	1913	1927	1918	1924	12.5	0.6	1.3
B4	2002	1998	1933	1950	1957	1956	1960	1881	1923	1912	1905	1892	1916	1905	15.7	0.8	1.6
B5	1951	1939	1896	1938	1932	1930	1920	1903	1881	1871	1873	1804	1860	1865	33.3	1.8	3.6
C1	2007	2023	1987	1986	2006	1890	1949	1900	1912	1935	1939	1937	1929	1925	15.8	0.8	1.6
C2	2042	2037	1977	1982	2000	1934	1976	1919	1940	1851	1921	1900	1918	1908	30.7	1.6	3.2
C3	2014	2008	1981	1953	1961	1915	1949	1945	1914	1879	1913	1937	1882	1912	27.2	1.4	2.8
C4	1966	1901	1918	1930	1890	1861	1915	1859	1792	1844	1810	1814	1806	1821	25.3	1.4	2.8
C5	2055	2044	2014	2010	2012	1970	1984	1967	1956	1978	1970	1980	1961	1969	9.4	0.5	1.0
D1	1961	1952	1939	1961	1972	1946	1885	1865	1865	1873	1842	1873	1879	1866	13.0	0.7	1.4
D2	2006	1976	1973	1958	1971	1955	1908	1910	1910	1907	1876	1861	1889	1892	20.5	1.1	2.2
D3	2077	2016	2010	2024	2028	2008	2022	1928	1950	1971	1955	1971	1968	1957	16.8	0.9	1.7
D4	1415	1356	1378	1384	1346	1305	1316	1314	1348	1303	1318	1304	1295	1314	18.7	1.4	2.8
D5	1997	2020	1958	2033	2047	2015	1979	1912	1963	1961	1904	1982	1923	1941	31.9	1.6	3.3
E1	2083	2084	1969	2014	2038	2007	2000	1978	1900	1981	1960	1962	1960	1957	29.4	1.5	3.0
E2	1985	1974	1918	1932	1905	1926	1903	1842	1862	1894	1872	1855	1905	1872	23.9	1.3	2.6
E3	2071	2049	2021	2007	1988	1973	2024	1954	1972	1954	1941	1955	1957	1955	9.9	0.5	1.0
E4	2035	2029	2000	1994	1981	1975	1974	1950	1939	1929	1890	1901	1940	1925	23.9	1.2	2.5
E5	1709	1750	1741	1707	1685	1732	1789	1661	1752	1705	1735	1638	1752	1707	28.2	1.7	3.3
Average	*1942*	*1936*	*1909*	*1912*	*1914*	*1888*	*1893*	*1853*	*1851*	*1851*	*1847*	*1844*	*1847*	*1849*			

Table 4.1 Readings for 25 TLD rods exposed to a constant dose (100 cGy each time) in a series of 13 consecutive experiments to investigate the variation of sensitivity.

eliminate the uncertainty in the exact dose given by such a small irradiation time, a special experimental arrangement was used to calibrate the TLDs.

As illustrated in figure 4.5, while the TLDs were positioned at a depth of 10 cm, an ionisation chamber was positioned at a depth of 14.3 cm. Under these circumstances, we do not only rely on the MU setting of the linac but we measure the dose at the same time that the TLDs are irradiated. Under these conditions, the dose given to the TLDs, D_{TLD}, is given by

$$D_{TLD} = MN_D P_{TP} P_s f_{poly} \frac{PDD(5.8)}{PDD(14.3)} \frac{PDD(10)}{100} \left(\frac{\mu_{abs}}{\rho} \right)_{water}^{poly} \qquad (4.1)$$

where M is the charge (nC) measured by the electrometer, N_D is the absorbed dose in water per unit signal of the electrometer (cGy/nC), P_{TP} is the factor that corrects for the temperature and pressure, P_S is the factor that corrects for recombination losses into the ion chamber, f_{poly} is the factor that converts a measurement taken at a depth of 5.8 cm in the plastic phantom to the dose that is obtained at D_{max} in water, $PDD(d)$ is the percent depth dose at the depth d, in cm, and $(\mu_{abs}/\rho)_{water}^{poly}$ is the ratio of the mass energy absorption coefficient of polystyrene to the one of water.

The TLD rods were periodically calibrated, and the calibration factor used for a given set of measurements was taken as the average of the last three or four calibrations. As discussed in section 4.3.3.7 above, a correction was also made to the calibration factor of the TLDs to account for the difference between the mean photon energy of the 6 MV photon beam and the mean photon energy of the radiation produced by the Ir-192 source.

As explained above, for the characterization of the low dose-rate Ir-192 source, the duration of the irradiation was set in such a way that the total dose integrated by the TLDs was approximately 7 cGy, which was the dose given to the TLDs during calibration. For these measurements, the background contribution to the total TLD signals was removed using the deconvolution routine mentioned in sub-section 4.3.2. For the characterization of the high dose-rate Ir-192 source, a total dose of approximately 100 cGy was given to the TLDs, because this dose coresponded to an appropriate irradiation duration time. The TLDs were therefore recalibrated at the new dose of 100 cGy. At this dose level, the background contribution to the total TLD signal was not subtracted with the aid of the deconvolution routine because it was determined to be unnecessary.

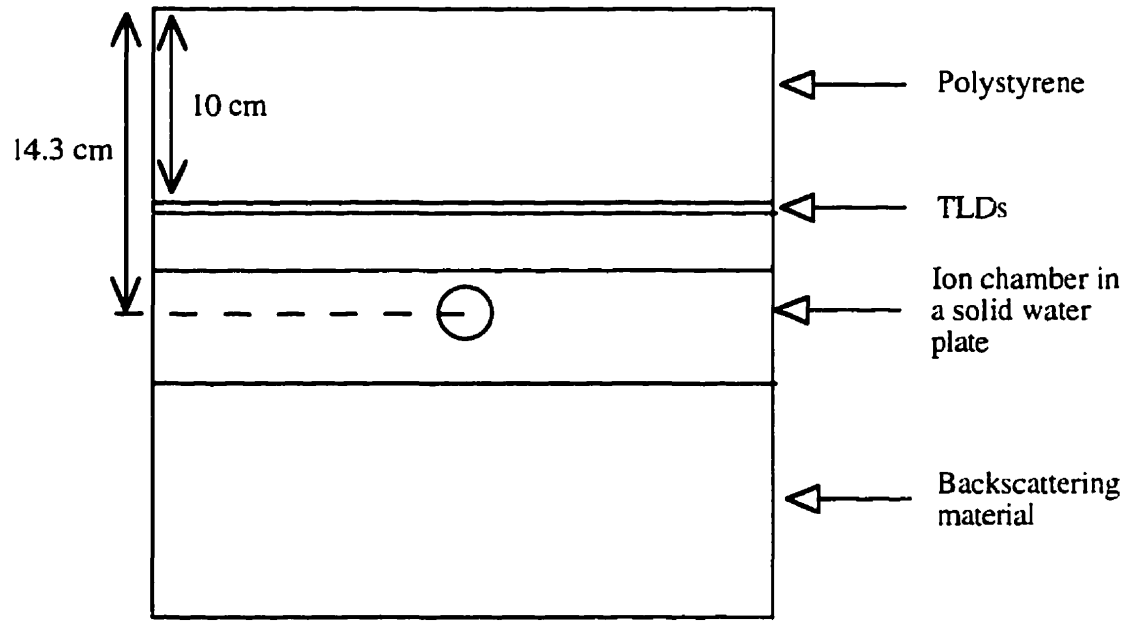

Figure 4.5 Positioning of TLDs and the ionization chamber for the calibration procedure.

4.3.3.4 Inter-detector Shielding Effect

A correction factor that authors sometimes mention in TLD-based experimental procedures arises from the interrod shielding effect. This effect occurs when some TLD rods are in the shadow of other rods. Since the attenuation and scattering characteristics of a TLD might be different from the same characteristics of the phantom material, erroneous results can be obtained. However, because of the design of the puzzle phantom, TLDs are always in direct line with the source and no such correction factor is required in our study.

4.3.3.5 Inter-detector Scattering Effect

Another effect to consider is the interrod scattering effect. This effect takes place when TLD detectors are positioned in close proximity during the measurement process. It is incorrect to assume that the scattering produced by neighbour TLD rods are necessarily the same as the scattering produced by a uniform medium. Since in our case we want to measure the anisotropy of the Ir-192 sources at every 10° of angular coverage, we do have

TLDs in close proximity with other ones, especially for distances equal to 1 and 2 cm from the source. To determine the interrod scattering effect for our experimental arrangement, special inner pieces were machined.

An inner piece was machined with two holes (instead of eight holes) at 1 cm from the source; a first hole at 0° and a second at 90°. We compared results obtained with this special inner piece placed into the puzzle phantom (which suffers very little from scattering disruption) to the results obtained, at the same angles, with the inner pieces of plastic perforated at every 20°. The interrod correction factor is then the ratio of the response of the isolated TLDs to that of their more densely packed coresponding detectors.

An irradiation time of 15 seconds, using the Microselectron HDR unit, was set to get a dose close to 100 cGy at the TLD position 1 cm, +90°. The average of eight successive measurements performed at the position 1 cm, +90° gave 97.8 cGy with the special inner piece that virtually eliminates any inter-detector scattering effect. The experiment was repeated with the regular inner piece that has TLD rods at every 20° and the average of eight successive measurements gave 97.9 cGy.

A second inner piece was also machined for a source-TLD distance of 2 cm and angles of 0° and 90°, and a similar experiment was performed. This time, an irradiation time of 60 seconds was used at the Microselectron HDR unit. The average of eight successive measurements performed at the position 2 cm, +90° gave 102.3 cGy with the special inner piece that virtually eliminates any inter-detector scattering effect. The experiment was repeated with the regular inner piece that has TLD rods at every 20° and the average of eight successive measurements gave 102.9 cGy.

We concluded that, within the limit of our experimental procedure, there was no inter-detector scattering correction factor required at distances of 1 cm and 2 cm.

It was determined to be unnecessary to perform similar measurements at larger distances, since the inter-detector scattering effect would be even smaller than at the distance equal to 1 cm.

4.3.3.6 Volume-averaging Correction Factor

Another correction factor is the volume-averaging or displacement correction factor. This factor is the ratio of dose at the geometric centre of detector to that averaged over the detector volume. Several authors (Gillin *et al.* 1988, Meigooni *et al.* 1988a, Luxton *et al.* 1990) have proposed various expressions for this correction factor. While some of the correction factors proposed by some authors are obtained through numerical integration, the correction factor proposed by Meigooni is derived from geometrical considerations and can be evaluated for any detector size and for any distance from the source. This correction factor, K, is defined by $K = \left[1 + (\Delta R/\sqrt{3}R)^2\right]$, where ΔR is the thickness of the detector and R is the distance between the center of the source and the center of the detector (this correction factor is incorrectly presented in the appendix of the original paper by Meigooni, due to a typographical error).

Within this study, we used TLD rods of 1 mm x 1 mm of cross-sectional dimension, positioned into 1.5-mm diameter receptacles perforated into the phantom. With ΔR equals to 1.5 mm, the largest correction factor, K, is at a distance of 1 cm, and is equal to 1.008.

4.3.3.7 TLD Sensitivity Variation with Mean Photon Energy

As a result of Compton scattering, the photon spectrum produced by an Ir-192 brachytherapy source shifts significantly toward lower energies with increasing distance in a phantom. For instance, as reported by Meigooni *et al.* (1988b), the mean photon energy in a polystyrene phantom varies from 335 keV at 1 cm to 216 keV at 10 cm. This variation of the mean photon energy causes the sensitivity of the TLDs to also vary as a function of the distance from the source. The same authors (Meigooni *et al.* 1988b) have used Monte Carlo calculations to determine the relative sensitivity of LiF TLDs at depths of 1, 5 and 10 cm inside a polystyrene phantom exposed to an Ir-192 source as compared to the sensitivity to a 4 MV x-ray beam. Figure 4.6 presents the results of a linear best fit of those data to determine the relative sensitivity of our detectors, for all the distances of interest for this study. We see that the sensitivity of TLDs increases by almost 6% from 1 cm to 10 cm (or from 335 keV to 216 keV) and the sensitivity of TLDs is approximately 1.5% higher for a photon mean energy equal to 335 kev (at 1 cm) as compared to the sensitivity of the same TLDs irradiated by a 4 MV linac photon beam.

Within this study, as we have no access to a 4MV beam, we perform the calibration procedure using a 6 MV linac. The mean energy of the photon beam used in our project is therefore slightly larger than the mean energy of the photon beam used in Meigooni's simulation, but as the LiF TLD response is virtually the same under 4 MV linac or 6 MV linac photon beams, these values have been used in our study to correct for the variation of detector response with distance in phantom.

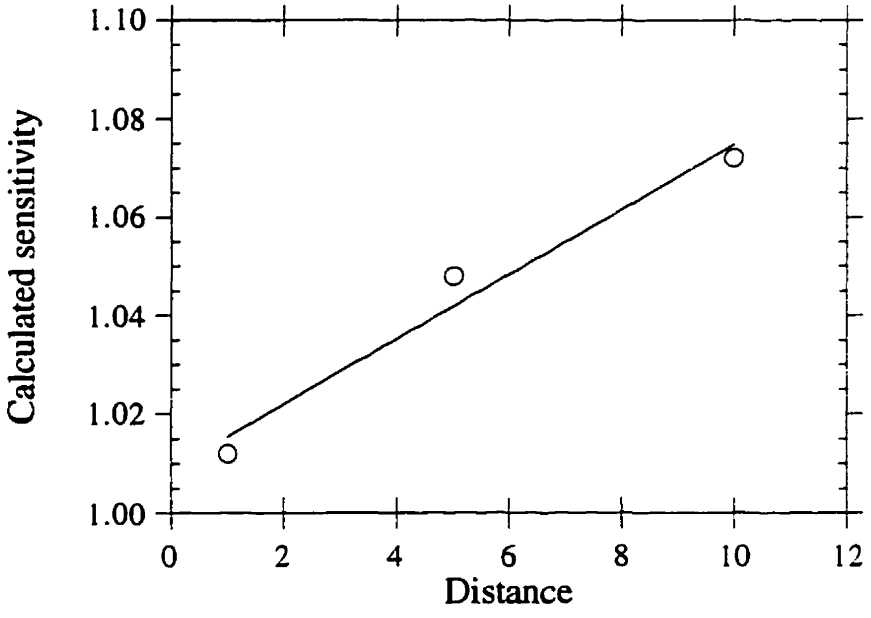

Figure 4.6 Relative sensitivity of TLDs as a function of the distance from the Ir-192 source in a polystyrene phantom (the sensitivity is normalized at 1.00 for a 4 MV linac photon beam).

4.4 Description and Use of the Iridium-192 Sources

Ir-192 is formed in a nuclear reactor by the activation of stable Ir-191 with thermal neutrons. Ir-192 decays in two ways. The most frequent disintegration of Ir-192 is through β^- emission to an excited state of Pt-192. Less frequently, Ir-192 decays by electron capture to an excited state of Os-192. The excited nuclei emit gamma rays of different energies. Table 2.1 presented above the most important transitions of the radionuclide. Estimates of the half-life of Ir-192 range from 73.8 days (Podgorsak 1993b)

to 74.2 days (Lederer and Shirley 1978). The manufacturer of the Microselectron high dose-rate afterloader, Nucletron Corporation, uses a value of 74.0 days as the half-life of its sources in the unit software.

4.4.1 Iridium-192 Low Dose-rate Sources

The Ir-192 low dose-rate (LDR) sources used within this research project are manufactured by Best Industries, Springfield, VA, USA.

4.4.1.1 Description of the LDR Ir-192 Source

Figure 4.7 shows a diagram of a LDR Ir-192 source. The seed is about 3 mm long and 0.5 mm in diameter, and is delivered to the user in a nylon ribbon. The internal configuration of the source consists of a 0.1-mm diameter core of 30% Ir and 70% Pt surrounded by a 0.2-mm thick stainless steel wall. The cladding serves to absorb beta radiation. An LDR source can have an initial strength of up to about 70 cGy cm^2 h^{-1} (650 MBq or 17 mCi).

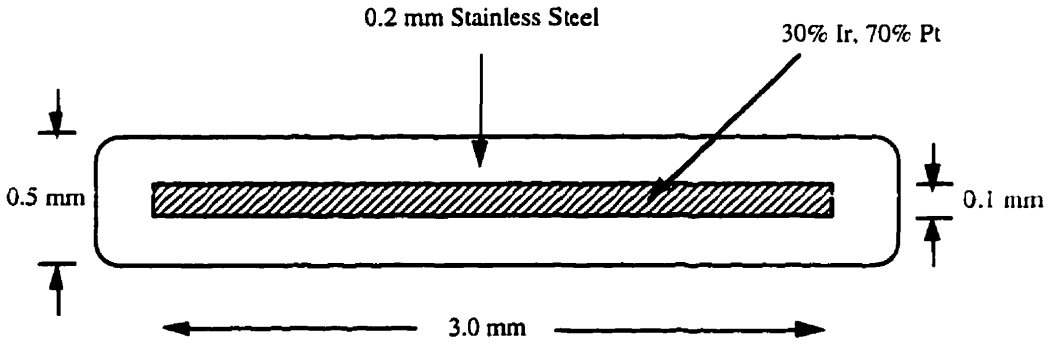

Figure 4.7 Diagram of a low dose-rate Ir-192 source.

4.4.1.2 Measurement Schedule with the LDR Ir-192 Source

The initial air kerma strength of the particular LDR source that was used for this study was approximately equal to 14 cGy cm^2 h^{-1} (3.4 mCi), as measured using a well-type ionization chamber (Goetsch *et al.* 1991, Ezzell 1993). Once the full set of measurements was completed, the source strength had decreased to about 5 cGy cm^2 h^{-1}.

To obtain the same total dose integrated by the TLDs, the irradiation time was varied as a function of the distance that separated the TLD rods from the source. A total dose of 7 cGy was selected since it was then possible to have a glow curve that did not suffer too much of background signal artefacts, while providing us with a long but manageable irradiation time at the 10-cm distance.

Some preliminary irradiations were performed at various distances to estimate the irradiation time required to give about 7 cGy to the TLDs as if all the measurements were performed on a reference date, 27 October 1996 (table 4.2).

Distance (cm)	Irradiation time (hours)
1	0.4
2	2
3	4
4	7
5	10
6	16
7	22
8	26
9	36
10	43

Table 4.2 Irradiation time required to integrate 7 cGy with the TLDs as a function of the distance from the source, as if measurements were performed on a reference date.

To account for the decay of the source and obtain the same integrated dose, the duration of the irradiation had to be increased as the apparent activity of the source decreased. Since we wanted to always record the same dose, we had to multiply the irradiation times that appear in table 4.2 by a factor that increased with time. Therefore, to avoid excessive irradiation times, the sequence of measurements was programmed starting from the longest distance (10 cm) and ending with the smallest distance (1 cm). To save time, two sets of TLDs were used. Measurements for distances larger than 6 cm were therefore performed with no time interruption, that is a group of TLDs were irradiated while the second group of TLDs was annealed.

To achieve the required precision, it was decided that each set of measurements would be performed five times. When we also add the time involved in periodic calibration checks of TLDs and the use of films to determine the exact position of the source inside the phantom, we estimated that a period of more than three months would be required to complete the full set of measurements on the LDR source.

4.4.1.3 Alignment of the Ir-192 LDR Source

For the dose measurements, the LDR source was manually inserted into the endobronchial applicator fixed to the puzzle phantom.

To maximise the precision of results, the distance between the source and the detectors had to be accurately determined. While results obtained at a souce-to-detector distance of more than 5 cm might not appreciably suffer from positioning error, because of the effect of the inverse square law, an error in positioning of only 300 μm for a source-to-detector distance of 1 cm imposes a six percent error in the evaluation of the anisotropy function at that distance, in addition to the other possible experimental errors. The use of the control TLD rod positioned at the coordinate 1 cm, -90° gave us the capability to correct for transverse positioning error.

To minimise this error in longitudinal positioning, radiographs were taken of the source inside the puzzle phantom as follows. The source was inserted into the endobronchial applicator and a special inner piece that consisted of only two holes at a distance of 1 cm, respectively at the 0° and 90° angular positions was used. Three small metal pieces were inserted at the angular positions 0°, +90° and -90°. A radiograph of the phantom was then taken, using an orthovoltage unit and used to position the source such that a straight line drawn on the film from the +90° TLD to the -90° TLD divided the source into two equal halves (figure 4.8). Using this technique, it is estimated that the error in the longitudinal positioning of the source was less than approximately 250 μm.

4.4.2 Iridium-192 High Dose-rate Sources

For the Ir-192 high dose-rate (HDR) source characterization, the Nucletron Microselectron HDR afterloader (Nucletron Corporation, Leersum, Holland) was used. The Microselectron HDR unit is a brachytherapy device that is designed to load HDR sources by remote control into pre-implanted applicators.

Figure 4.8 Radiograph of the low dose-rate Ir-192 source inside the puzzle phantom showing the technique used to adjust for the longitudinal positioning of the source.

4.4.2.1 Description of the HDR Ir-192 Source

Figure 4.9 shows a diagram of a HDR Ir-192 source. The Ir-192 sources used in the Microselectron HDR afterloader are approximately 5 mm long and 1.1 mm in diameter, and are attached to a stainless steel cable connected to stepping motors that can precisely position the source into the applicators. The internal configuration of the sources consist of a 3.5-mm long, 0.6-mm diameter core surrounded by a 0.25-mm thick stainless steel wall. A typical HDR source has an initial strength of about 41,000 cGy cm^2 h^{-1} (370 GBq or 10 Ci).

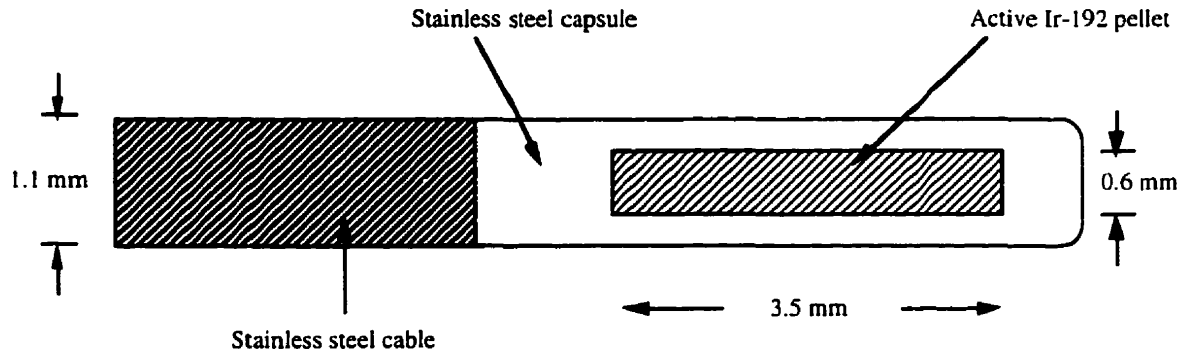

Figure 4.9 Diagram to illustrate the structure of an HDR Ir-192 source.

To take the series of measurements required to obtain the dosimetric functions of the TG 43 protocol, the HDR source was positioned into the endobronchial applicator fixed to the puzzle phantom with the aid of the Microselectron programmable controller. The controller provides the user with the possibility to position the source into the applicator using 48 dwell positions separated by 2.5 or 5.0 mm, the most distal position being 995 mm from the treatment unit. The dwell time can be set to any value between 0.1 and 999.9 seconds.

4.4.2.2 Measurement Schedule with the HDR Ir-192 Source

The particular HDR source that was used within this study had an initial strength of about 28,000 cGy cm^2 h^{-1} (250 GBq or 6.8 Ci). Once the full set of measurements was completed, the source strength had decreased to about 17,000 cGy cm^2 h^{-1} (150 GBq or 4.2 Ci).

To characterize the HDR source, the TLDs were calibrated at a dose of about 100 cGy, since this corresponded to a dose that could be integrated by our TLDs for a practical time duration of irradiation (a smaller dose would have required a too short irradiation time at 1 cm). The irradiation time required to give about 100 cGy to the TLDs at various distances, at a reference date, 20 February 1997, is given in table 4.3.

To account for the decay of the source and obtain the same integrated dose, the duration of the irradiation had to be increased as the apparent activity of the source decreased. Moreover, it was advantageous to start with the measurements at the longer

distances, since we wanted to avoid as much as possible inserting the source twice for a given set of measurements which would be required for any exposure time greater than 999.9 s. This procedure also reduced the effect of the transit dose for the measurements performed at the smaller distances.

Distance (cm)	Irradiation time (s)
1	11.5
2	46
3	103
4	184
5	287
6	414
7	593
8	775
9	1012
10	1278

Table 4.3 Irradiation time required to integrate 100 cGy with the TLDs as a function of the distance from the source, assuming measurements were all performed on a reference date.

4.4.2.3 Alignment of the Ir-192 HDR Source

Similarly to the case of the low dose-rate source, the distance between the HDR Ir-192 source and the detectors has to be accurately determined.

The positioning of the source was performed by taking first an autoradiograph of the HDR source inside the puzzle phantom, followed by a radiograph of the phantom with three small metal pieces inserted at a distance of 1 cm and at angular positions 0°, +90° and -90°. The radiograph of the phantom was taken with an orthovoltage unit. Figure 4.10 is a photo of the radiograph obtained once the position of the applicator was adjusted to center the source in such a way that a straight line drawn on the film from the +90° TLD position to the -90° TLD position divided the source into two equal halves. Using this technique, it is estimated that the error in the longitudinal positioning of the soure is not less than approximately 250 μm.

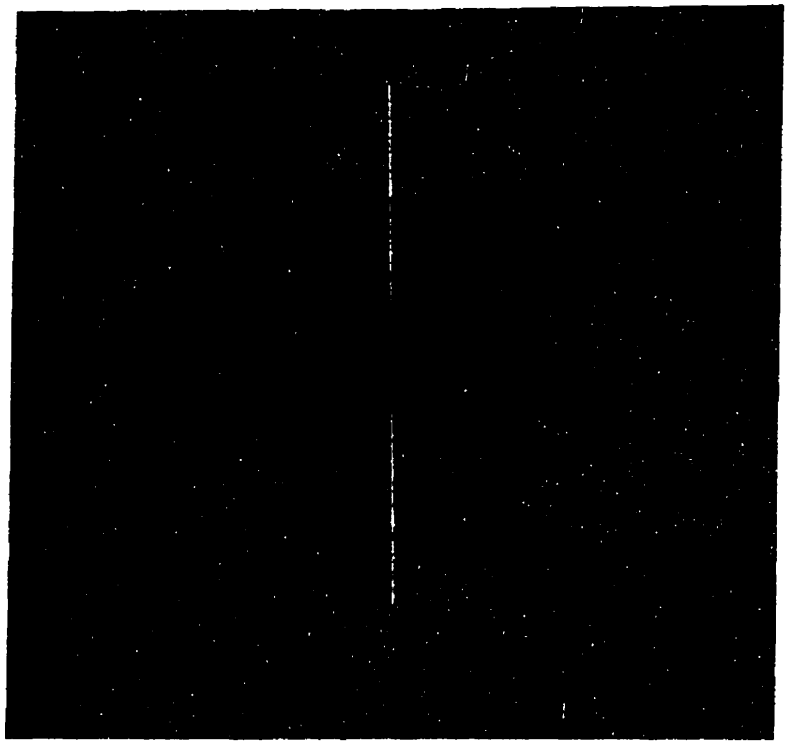

Figure 4.10 Radiograph of the high dose-rate Ir-192 source inside the puzzle phantom showing the technique used to adjust for the longitudinal positioning of the source.

4.5 Transit Dose

The dose rates of interest in this study are the dose rates produced from the stationary source position (r = 0). However, the dose rate of the HDR Ir-192 source is so high that, when the source travels, a transit dose is integrated by the TLDs and this transit dose has to be estimated and substracted from the results.

The clinical impact of the transit dose has been lately discussed by several investigators. Houdek *et al.* (1992) has developed a formalism that describes both the dynamic as well as the stationary components of HDR treatments. Bastin et al. (1993) have also used TLDs to measure the transit dose produced by an HDR afterloading source for distances that varied between 0.5 cm and 4.0 cm. However our geometical configuration was very different from the configuration used by other investigators and we

could not use their results to estimate the transit dose integrated by our TLDs. The transit dose was then measured for all distances and angles where experimental results were taken.

For the larger radii (≥ 5 cm), using the TLDs that were calibrated at a lower dose level (7 cGy), the source was introduced 4 or 5 times with the programmed minimum stay time of the HDR source (0.1 sec). The transit dose was then approximately equal to the value obtained divided by the number of times the source was inserted.

For smaller radii, the dose rate, *DR*, in cGy sec^{-1}, at every point was determined by dividing the dose integrated over a relatively long time (> 20 sec for example) by the time of irradiation. The source was then inserted during 0.1 sec and the small dose, *SD*, is measured. The transit dose, *TD*, was then given by

$$TD = SD - DR \times 0.1 \qquad (4.2)$$

The transit doses were determined experimentally for all distances and angles. Some illustrative results are shown in table 4.4.

Transit Dose Values (cGy)			
Angle	**at r=2 cm**	**at r=6 cm**	**at r=10 cm**
0°	~ 0.1	< 0.1	< 0.1
10°	~ 0.1	< 0.1	< 0.1
20°	~ 0.1	< 0.1	< 0.1
30°	~ 0.1	< 0.1	< 0.1
40°	~ 0.1	< 0.1	< 0.1
50°	~ 0.1	< 0.1	< 0.1
60°	~ 0.1	< 0.1	< 0.1
70°	~ 0.2	< 0.1	< 0.1
80°	~ 0.2	~ 0.1	< 0.1
90°	~ 0.2	~ 0.1	< 0.1
100°	~ 0.2	~ 0.1	< 0.1
110°	~ 0.3	~ 0.1	< 0.1
120°	~ 0.4	~ 0.1	< 0.1
130°	~ 0.5	~ 0.1	< 0.1
140°	~ 0.6	~ 0.2	< 0.1
150°	~ 0.8	~ 0.2	~ 0.3
160°	~ 1.3	~ 0.4	~ 0.5
170°		~ 0.8	~ 1.0

Table 4.4 Transit doses measured for all angles and distances of 2, 6 and 10 cm.

Table 4.4 illustrates that for the larger radii, the transit dose is larger than 0.1 cGy only for the TLDs that are positioned at angles larger than 140°. For the smaller radii, more TLDs integrate a transit dose larger than 0.1 cGy because the distance is shorter. Moreover, table 4.4 illustrates that even though the TLD positioned at 6 cm, 170° is closer (~10 mm) to the source path (endobronchial applicator) than the TLD positioned at 10 cm, 170° (~17 mm), its transit dose is smaller because the source needs to be inserted only once when performing measurements at the 6-cm distance but the source must be inserted twice at the 10-cm distance, since the required dwell time at the latter distance is more than 999.9 seconds (table 4.3). The values obtained by these two procedures were substracted from the experimentally obtained doses to determine the doses that correspond to the stationary source position.

4.6 Measurement Procedures

4.6.1 Procedures to Determine the Anisotropy Function

The puzzle phantom was designed to measure the anisotropy function of brachytherapy sources through a series of dose-rate measurements taken by positioning detectors at a single distance but at all angles of interest at one time. Since each anisotropy function is normalized to 1.000 at the 90° angular position, the anisotropy functions obtained on a given source but at different distances can be compared even though measurements can be separated by several days or weeks.

4.6.2 Procedures to Determine the Radial Dose Function

The anisotropy results can also be used to determine the radial dose functions but the data must be transformed to account for the TLD volume averaging effect, the variation of the sensitivity of the TLDs as a function of distance and the decay of the source between each sets of measurements. In the case of the low-dose rate Ir-192 source, the duration time of the irradiation procedure has also to be taken into account.

For each series of measurements, the date and time of the start and the total duration of the irradiation were recorded. Since the integrated dose is measured with TLDs, we can find the dose rate being measured by the detectors at the beginning of the irradiation process and this dose rate can be used to find a dose rate that would have been measured at

an arbitrary date. In practice, the fifty doses obtained at the 90° angular position (10 distances, 5 measurements at each distance) for each brachytherapy sources were transformed to dose rates on a reference date (1 October 1996 for the LDR source and 21 February 1997 for the HDR source) by multiplying the dose rate obtained at a given day by $e^{\lambda t}$ where λ is the decay constant and t is the number of days between the measurement and the reference date.

The dose rate is equal to the integrated dose divided by the irradiation time only when the irradiation time is very small as compared to the half life of the source. In general terms, the dose rate is given by:

$$\dot{D}_0 = \frac{Dose \times \lambda}{1 - e^{-\lambda t}} \qquad (4.3)$$

where λ is the decay constant and t is the total duration time of irradiation. The use of equation 4.3 was required to analyse the results obtained with the low dose-rate source. For the high dose-rate source, the dose rate was simply given by the ratio of the measured dose by the time duration of the irradiation process.

The method discussed in Chapters 3 and 4 was then used to determine the radial dose function. Equation 3.8, which gives the radial dose function, $g(r)$, from dose rates measured on the transverse axis of the source and geometry factors was used, but only after the two dose rates were modified to account for the TLDs volume-averaging effect (discussed in section 4.3.3.6) and the TLDs sensitivity variation with distance (discussed in section 4.3.3.7).

4.6.3 Procedures to Determine the Dose Rate Constant

As seen in equation 3.13, the dose rate constant is obtained by measuring the dose rate at 1 cm, 90°, and the source strength, S_k. The positioning error of the TLD rod can be virtually eliminated by taking the average of readings obtained at the same time at the positions 1 cm, +90° and 1 cm, -90°, as explained in section 4.2.2. To improve the precision in the results, more than 20 measurements, performed on several different days, were averaged to obtain the best estimate of the dose rate constant.

4.7 Estimates of Experimental Errors

This section presents the estimate of the errors associated with the experimental results obtained within this study. The present discussion of error analysis follows the method presented in Chapter 3 of Bevington and Robinson (1992).

4.7.1 General Considerations

In experimental physics, a dependent variable x is often a function of one or more different measured quantities. We therefore need to determine the uncertainty in the dependent variable due to the uncertainties in the measured variables. To determine the uncertainty in the result, we have first to estimate the error in each measured quantity, or to estimate some characteristic, such as the standard deviation σ, of the probability distribution of the measured quantities and then combine the error or standard deviation of the individual measurements.

Let us suppose that we have a quantity x which is a function of at least two measured variables, u and v, or

$$x = f(u, v, \ldots) \tag{4.4}$$

The approximation of the variance σ_x^2 for x is given by

$$\sigma_x^2 = \sigma_u^2\left(\frac{\partial x}{\partial u}\right)^2 + \sigma_v^2\left(\frac{\partial x}{\partial v}\right)^2 + \ldots + 2\sigma_{uv}^2\left(\frac{\partial x}{\partial u}\right)\left(\frac{\partial x}{\partial v}\right) + \ldots \tag{4.5}$$

where σ_u^2 and σ_v^2 are the variances of the variables u and v, and σ_{uv}^2 are the covariances between the variables u and v. This equation is called the *error propagation equation*. The first two terms of equation 4.5 are averages of squares of deviations weighted by the squares of the partial derivatives. In general, these terms dominate the uncertainties. If there are more than two independent variables, the contribution of these extra variables to the variance of x will have similar terms. The third term in equation 4.5 is the average of the cross terms involving products of deviations in u and v. If the fluctuations in the measured quantities u and v are uncorrelated, this term can be neglected and the error propagation equation becomes:

$$\sigma_x^2 \approx \sigma_u^2\left(\frac{\partial x}{\partial u}\right)^2 + \sigma_v^2\left(\frac{\partial x}{\partial v}\right)^2 + \ldots \qquad (4.6)$$

For instance, for the common cases where x is the weighted product of u and v, that is

$$x = auv \qquad (4.7)$$

or when x is obtained through division, that is

$$x = \frac{au}{v} \qquad (4.8)$$

the application of equation 4.6 then gives that the variance for x is given, in both cases, by:

$$\frac{\sigma_x^2}{x^2} = \frac{\sigma_u^2}{u^2} + \frac{\sigma_v^2}{v^2} \qquad (4.9)$$

For these cases, the uncertainties are said to be added in quadrature.

4.7.2 Uncertainties Related to our Experimental Results.

This section presents an estimate of the total error associated to the three main functions and factors obtained in this study, that is the anisotropy function, $F(r,\theta)$, the radial function, $g(r)$, and the dose rate constant, Λ.

4.7.2.1 Errors in the Measurement of the Anisotropy Function

The determination of the anisotropy function $F(r,\theta)$ suffers from uncertainties in the individual response of TLDs and positioning errors. It does not suffer from the estimate of the TLD response variation with distance nor from the estimate of the volume correction factor because the anisotropy function is obtained through ratios of TLD readings all obtained at the same distance from the source.

From table 4.1, we conclude that an error equal to or less than 3% can be associated with an individual TLD reading. Since each measurement is performed five times, the error is reduced by the square root of five, therefore the error of a dose measurement at a given position can be estimated at about 1.3%.

The error associated with the positioning error varies as a function of the distance from the source. The error in positioning is constant in absolute value, therefore it is larger in percentage for the results obtained at one or two centimeters than for the results obtained at larger distances. Furthermore, at distances of 1 cm and 2 cm, the use of a control TLD at the 1cm,-90° position greatly reduces the transverse positioning error but does not correct for the longitudinal positioning error. At one and two centimeters the positioning error is therefore a function of the angle. If we consider that correction, and if we assume, as stated above, that the longitudinal positioning error is about 0.25 mm, for both the LDR and the HDR source, the error estimates associated with positioning only were obtained and are presented in table 4.5. In this table, it was assumed that the total positioning error is about 0.25 mm at any angular position for distances larger than 2 cm.

	Distances				
Angles	**1 cm**	**2 cm**	**3 cm**	**4 cm**	**≥ 5 cm**
0°	~ 5.0	~ 2.5	~ 1.7	~ 1.3	≤ 1
10° and 170°	~ 4.9	~ 2.5	~ 1.7	~ 1.3	≤ 1
20° and 160°	~ 4.7	~ 2.3	~ 1.7	~ 1.3	≤ 1
30° and 150°	~ 4.3	~ 2.2	~ 1.7	~ 1.3	≤ 1
40° and 140°	~ 3.8	~ 1.9	~ 1.7	~ 1.3	≤ 1
50° and 130°	~ 3.2	~ 1.6	~ 1.7	~ 1.3	≤ 1
60° and 120°	~ 2.5	~ 1.2	~ 1.7	~ 1.3	≤ 1
70° and 110°	~ 1.7	~ 0.9	~ 1.7	~ 1.3	≤ 1
80° and 100°	~ 0.9	~ 0.4	~ 1.7	~ 1.3	≤ 1
90°	~ 0	~ 0	~ 1.7	~ 1.3	≤ 1

Table 4.5 Estimate of the error incurred in the TLD readings (%) due to the uncertainty in the longitudinal position of the source.

When we add in quadrature the positioning error to the error associated with the TLD signals, we obtain the total error estimates shown in table 4.6.

Angles	Distances				
	1 cm	2 cm	3 cm	4 cm	≥ 5 cm
0°	~ 5.2	~ 2.8	~ 2.1	~ 1.8	≤ 1.6
10° and 170°	~ 5.1	~ 2.8	~ 2.1	~ 1.8	≤ 1.6
20° and 160°	~ 4.9	~ 2.6	~ 2.1	~ 1.8	≤ 1.6
30° and 150°	~ 4.5	~ 2.6	~ 2.1	~ 1.8	≤ 1.6
40° and 140°	~ 4.0	~ 2.3	~ 2.1	~ 1.8	≤ 1.6
50° and 130°	~ 3.5	~ 2.1	~ 2.1	~ 1.8	≤ 1.6
60° and 120°	~ 2.8	~ 1.8	~ 2.1	~ 1.8	≤ 1.6
70° and 110°	~ 2.1	~ 1.6	~ 2.1	~ 1.8	≤ 1.6
80° and 100°	~ 1.6	~ 1.4	~ 2.1	~ 1.8	≤ 1.6
90°	~ 1.3	~ 1.3	~ 2.1	~ 1.8	≤ 1.6

Table 4.6 Estimate of the error incurred in the TLD readings (%) due to the uncertainty in the positioning of the source and to the individual response of TLDs.

Since the values of the anisotropy function, $F(r,\theta)$, are obtained by the ratio of the signal obtained at a given distance over the signal obtained at the 1 cm-distance, the error estimates associated with the radial dose function will be modified accordingly and are given in table 4.7.

As shown in table 4.7, there is no error estimate associated with the value of the anisotropy function at 90° since it is then set at 1.000 by definition. These error estimates were used to establish the errors indicated in tables 5.1, 5.2, 5.6 and 5.7 and the error bars in figures 5.1, 5.3, 5.5, 5.7 and 6.3.

Angles	Distances				
	1 cm	2 cm	3 cm	4 cm	≥ 5 cm
0°	~ 5.4	~ 3.1	~ 2.5	~ 2.2	≤ 2.1
10° and 170°	~ 5.3	~ 3.1	~ 2.5	~ 2.2	≤ 2.1
20° and 160°	~ 5.1	~ 2.9	~ 2.5	~ 2.2	≤ 2.1
30° and 150°	~ 4.7	~ 2.9	~ 2.5	~ 2.2	≤ 2.1
40° and 140°	~ 4.2	~ 2.6	~ 2.5	~ 2.2	≤ 2.1
50° and 130°	~ 3.7	~ 2.5	~ 2.5	~ 2.2	≤ 2.1
60° and 120°	~ 3.1	~ 2.2	~ 2.5	~ 2.2	≤ 2.1
70° and 110°	~ 2.5	~ 2.1	~ 2.5	~ 2.2	≤ 2.1
80° and 100°	~ 2.1	~ 1.9	~ 2.5	~ 2.2	≤ 2.1
90°	NA	NA	NA	NA	NA

Table 4.7 Error estimates (%) in the evaluation of the anisotropy function.

4.7.2.2 Errors in the Measurement of the Radial Dose Function

The determination of the radial dose function $g(r)$ suffers from uncertainties in the individual response of TLDs, positioning errors, errors in the estimate of the TLD sensitivity variation with distance and the error in the volume-averaging factor.

Using the same argument as in the previous section, the error due to the individual TLD response can be estimated at 1.3%.

The positioning errors can be neglected for the measurements at distances of 1 and 2 cm, since readings from the control TLD at the position 1cm,-90° have been used to compensate for possible positioning errors. For distances equal to 3 cm and 4 cm, the positioning error is estimated at respectively 1.7% and 1.3%. For distances equal or larger than 5 cm, the positioning error is estimated at 1% or less.

The TLD sensitivity factors that vary with distance were determined by a linear best fit of published Monte Carlo calculations. The error incurred by this procedure can be estimated at about one percent.

There are many ways to calculate the volume-averaging factor. Different authors have arrived at somewhat different factors. An uncertainty of about one percent can be assumed for this factor at a distance of 1 cm, but the uncertainty can be neglected for larger distances because all authors agree that the volume correction factor is then very close to unity.

When we add in quadrature these four error factors, the signal that we obtain at each distances has an estimated error given in table 4.8.

Distance (cm)	Error Estimate (%)
1	~ 1.9
2	~ 1.6
3	~ 2.4
4	~ 2.1
≥ 5	≤ 1.9

Table 4.8 Estimated error associated with the TLD measured signal as a function of distance.

Since the values of the radial dose function, $g(r)$, are obtained by the ratio of the signal obtained at a given distance over the signal obtained at the 1 cm-distance, the error estimates associated with the radial dose function will be modified accordingly and are given in table 4.9.

As indicated in table 4.9, there is no error estimate associated to the value of the radial dose function at a distance of 1 cm, since it is then set at 1.000 by definition. These error estimates were used in tables 5.5 and 5.10 and in figures 5.4, 5.8, 6.1 and 6.2.

Distance (cm)	Error Estimate (%)
1	Not applicable
2	~ 2.5
3	~ 3.1
4	~ 2.8
≥ 5	≤ 2.7

Table 4.9 Error estimates of the values obtained for the radial dose function.

4.7.2.3 Errors in the Measurement of the Dose Rate Constant

The determination of the dose rate constant, Λ, suffers from uncertainties in the individual response of TLDs, the error in the volume-averaging factor, positioning errors, errors in the estimate of the TLD calibration factor and the error in the measurement of the source strength.

Using the same argument as in previous sections, the error due to the individual TLD response can be estimated at 1.3%. Since the dose rate constant is estimated by averaging 24 measurements, the error due to TLD response is about 0.6%.

An error of about one percent can also be assumed for the volume-averaging factor.

The positioning errors can be neglected since the measurements are performed at the same time using a TLD at the position 1 cm, +90° and another TLD at the position 1 cm, -90°.

For the determination of the dose rate constant, Λ, we need the true dose rate obtained at a distance of 1 cm. Errors associated with physical constants, calibration of instruments and phantom setup are difficult to establish. However it is usual to estimate the overall uncertainty of a linac beam calibration, using current accepted procedures, at about 2.5% (ICRU 1976).

When we add in quadrature these four error factors, we obtain the error estimate on the measurement of the dose rate constant of about 2.9%. This uncertainty estimate was used in tables 6.2 and 6.3.

5.0 EXPERIMENTAL RESULTS

5.1 Characterization of the Low Dose-rate Ir-192 Source

5.1.1 Experimental Determination of the Anisotropy Function, $F(r,\theta)$

The first series of measurements were the determination of the anisotropy function at a distance of 10 cm (table 5.1).

Angles	Series #1	Series #2	Series #3	Series #4	Series #5	Average
0°	0.886	0.852	0.892	0.908	0.891	0.886 ± 0.019
10°	0.928	0.934	0.911	0.944	0.932	0.930 ± 0.020
20°	0.961	0.974	0.953	0.942	0.945	0.955 ± 0.020
30°	0.986	0.969	0.964	0.982	0.959	0.972 ± 0.020
40°	0.965	0.960	0.947	0.962	0.960	0.959 ± 0.020
50°	0.993	0.957	1.006	1.009	1.006	0.994 ± 0.021
60°	1.000	0.978	0.987	0.992	0.997	0.991 ± 0.021
70°	0.975	1.003	1.011	0.995	1.009	0.999 ± 0.021
80°	0.987	1.000	1.006	0.989	0.981	0.993 ± 0.021
90°	1.000	1.000	1.000	1.000	1.000	1.000
100°	0.999	0.968	0.994	1.065	1.004	1.006 ± 0.021
110°	0.975	0.961	0.995	1.000	0.990	0.984 ± 0.021
120°	1.022	1.048	0.940	0.989	1.013	1.003 ± 0.021
130°	0.978	0.966	0.972	0.929	1.009	0.971 ± 0.020
140°	0.981	0.974	0.978	0.986	0.976	0.979 ± 0.021
150°	0.971	0.969	0.945	0.977	0.984	0.969 ± 0.020
160°	0.941	0.958	0.967	0.967	0.979	0.962 ± 0.020
170°	0.913	0.954	0.934	0.926	0.957	0.937 ± 0.020

Table 5.1 Series of values of the anisotropy function measured at a distance of 10 cm from the low dose-rate Iridium-192 source.

We see that the average of five sets of measurements does not produce a perfectly smooth anisotropy function. The average of the sets is however smoother than any of the individual series which demonstrates the need to repeat the experiment many times to obtain results with which we are confident. Results would be even smoother if we could add three or four more sets of measurements but this would add several months to the collection of experimental data. The anisotropy function of the low dose-rate Ir-192 source is graphically presented in figure 5.1. The solid line in figure 5.1 is a polynomial best fit to the experimental results. We see that self-attenuation of the radiation and attenuation inside

the cladding of the source reduces the value of *F(10 cm, 0°)* by about 12% as compared to the value of *F(10 cm, π/2)*. We also note a symmetrical behaviour of the anisotropy function around its value along the transverse axis of the source.

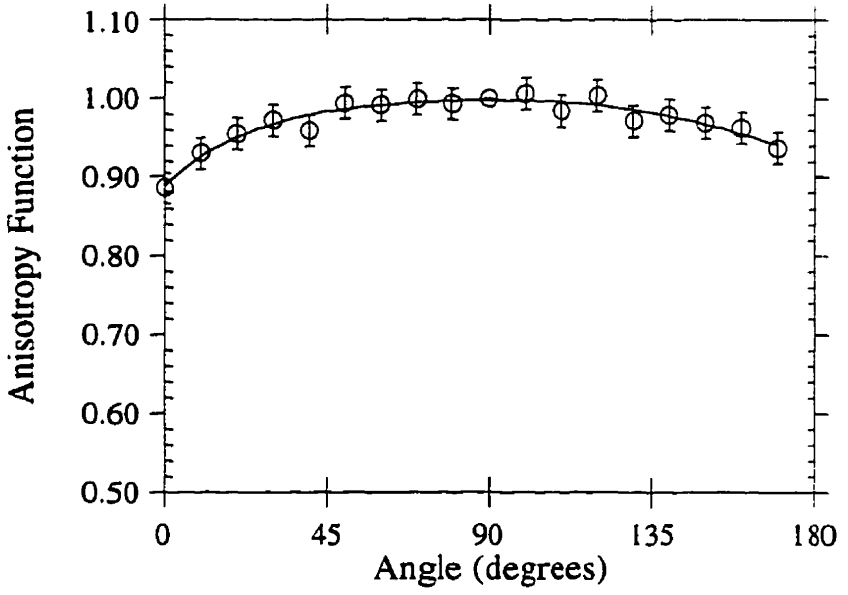

Figure 5.1- Anisotropy of the low dose-rate Ir-192 source at a distance of 10 cm.

The anisotropy factor, ϕ_{an}, corresponding to the results presented in table 5.1, as determined with the procedure presented in Section 3.7, is equal to 0.983.

The same procedure was used for the nine other distances of interest (table 5.2).

We see from table 5.2 that because of the design of the puzzle phantom, it was impossible to cover the 170° angle at distances of 2 and 3 cm, and the 150°, 160° and 170° angle at the 1-cm distance. Figure 5.2 gives a plot of the 10 anisotropy functions presented in table 5.2. Each minor Y-axis division in figure 5.2 represents a value of 0.1.

The anisotropy functions are relatively symmetrical around the transverse axis, especially for the larger distances where positioning errors are minimised.

Angles	Distances									
	1 cm	2 cm	3cm	4 cm	5 cm	6 cm	7 cm	8 cm	9 cm	10 cm
0°	0.817 ±0.044	0.852 ±0.026	0.836 ±0.021	0.827 ±0.018	0.852 ±0.018	0.879 ±0.019	0.860 ±0.018	0.884 ±0.019	0.883 ±0.019	0.886 ±0.019
10°	0.874 ±0.046	0.938 ±0.029	0.931 ±0.023	0.921 ±0.020	0.942 ±0.020	0.941 ±0.020	0.952 ±0.020	0.926 ±0.019	0.927 ±0.019	0.930 ±0.019
20°	0.914 ±0.047	0.973 ±0.028	0.967 ±0.024	0.946 ±0.021	0.963 ±0.020	0.957 ±0.020	0.969 ±0.020	0.965 ±0.020	0.937 ±0.020	0.955 ±0.020
30°	0.921 ±0.043	0.987 ±0.029	0.978 ±0.024	0.971 ±0.021	0.963 ±0.020	0.961 ±0.020	0.968 ±0.020	0.977 ±0.020	0.965 ±0.020	0.972 ±0.020
40°	0.940 ±0.039	0.998 ±0.026	0.986 ±0.025	0.991 ±0.022	0.989 ±0.021	0.987 ±0.021	0.984 ±0.021	0.974 ±0.020	0.964 ±0.020	0.959 ±0.020
50°	0.968 ±0.036	0.988 ±0.025	1.009 ±0.025	0.991 ±0.022	0.987 ±0.021	1.001 ±0.021	1.008 ±0.021	0.989 ±0.021	0.995 ±0.021	0.994 ±0.021
60°	0.953 ±0.029	0.993 ±0.022	1.013 ±0.025	0.995 ±0.022	1.000 ±0.021	0.999 ±0.021	1.006 ±0.021	0.991 ±0.021	0.976 ±0.020	0.991 ±0.021
70°	0.979 ±0.024	0.997 ±0.021	0.995 ±0.025	0.998 ±0.022	1.000 ±0.021	0.993 ±0.021	1.006 ±0.021	0.999 ±0.021	1.006 ±0.021	0.999 ±0.021
80°	0.988 ±0.021	1.007 ±0.019	1.004 ±0.025	1.000 ±0.022	0.987 ±0.021	1.001 ±0.021	0.984 ±0.021	0.987 ±0.021	0.983 ±0.021	0.993 ±0.021
90°	*1.000*	*1.000*	*1.000*	*1.000*	*1.000*	*1.000*	*1.000*	*1.000*	*1.000*	*1.000*
100°	1.013 ±0.021	0.992 ±0.019	0.999 ±0.025	0.992 ±0.022	0.998 ±0.021	0.992 ±0.021	1.000 ±0.021	0.999 ±0.021	0.986 ±0.021	1.006 ±0.021
110°	1.002 ±0.025	0.999 ±0.021	0.999 ±0.025	1.004 ±0.022	1.001 ±0.021	1.003 ±0.021	1.002 ±0.021	0.988 ±0.021	0.995 ±0.021	0.984 ±0.021
120°	0.996 ±0.031	0.991 ±0.022	0.990 ±0.025	0.991 ±0.022	1.000 ±0.021	0.991 ±0.021	1.007 ±0.021	1.000 ±0.021	0.986 ±0.021	1.003 ±0.021
130°	1.021 ±0.038	0.976 ±0.024	0.977 ±0.024	0.990 ±0.022	0.993 ±0.021	0.991 ±0.021	0.990 ±0.021	0.985 ±0.021	0.976 ±0.020	0.971 ±0.020
140°	1.007 ±0.042	0.977 ±0.025	0.986 ±0.025	0.981 ±0.022	0.980 ±0.021	0.975 ±0.020	0.992 ±0.021	0.978 ±0.021	0.968 ±0.020	0.979 ±0.021
150°		0.970 ±0.028	0.970 ±0.024	0.970 ±0.021	0.967 ±0.020	0.978 ±0.021	0.975 ±0.020	0.982 ±0.021	0.968 ±0.020	0.969 ±0.020
160°		0.947 ±0.027	0.961 ±0.024	0.966 ±0.021	0.956 ±0.020	0.957 ±0.020	0.972 ±0.020	0.969 ±0.020	0.960 ±0.020	0.962 ±0.020
170°				0.914 ±0.020	0.926 ±0.019	0.930 ±0.019	0.936 ±0.020	0.934 ±0.020	0.940 ±0.020	0.937 ±0.020

Table 5.2 Series of values of the anisotropy functions measured at distances from 1 to 10 cm from the low dose-rate Iridium-192 source.

The increased contribution of scattered photons to the dose as the distance from the source increases reduces the anisotropy seen at larger distances. To illustrate this effect, figure 5.3 presents a plot of the ten anisotropy function values at the 0° angular position, which is where the anisotropy of the source is maximum. The solid line is the linear best fit of the data points. We clearly see, despite the relatively large error on some data points, that the anisotropy reduces as the distance from the source increases. This characteristic

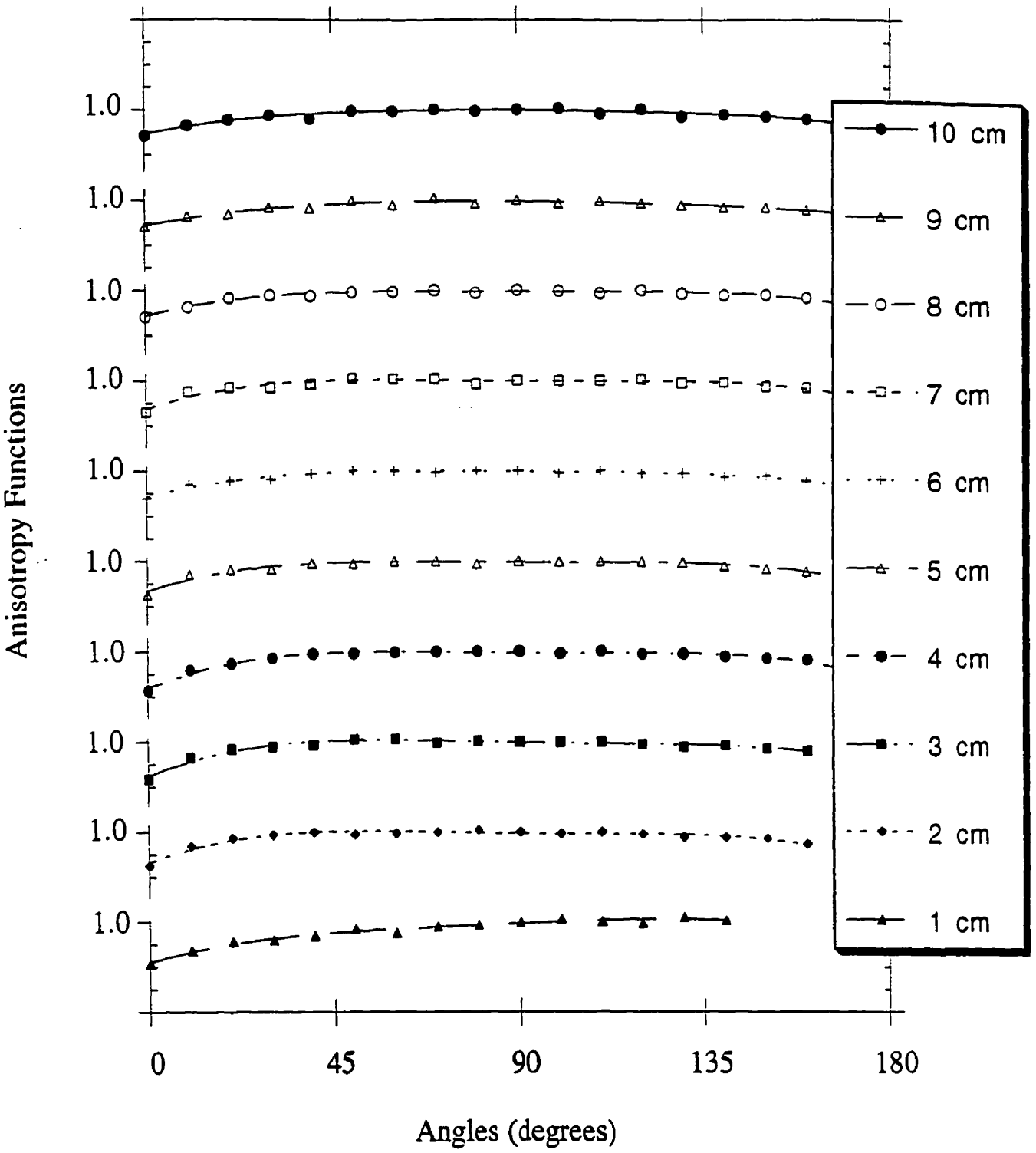

Figure 5.2 The complete anisotropy functions of the LDR Ir-192 source, with a modified ordinate axis. Each minor Y-axis division represents a value of 0.1.

has also been reported by Muller-Runkel and Cho (1994) for the case of an HDR Ir-192 source.

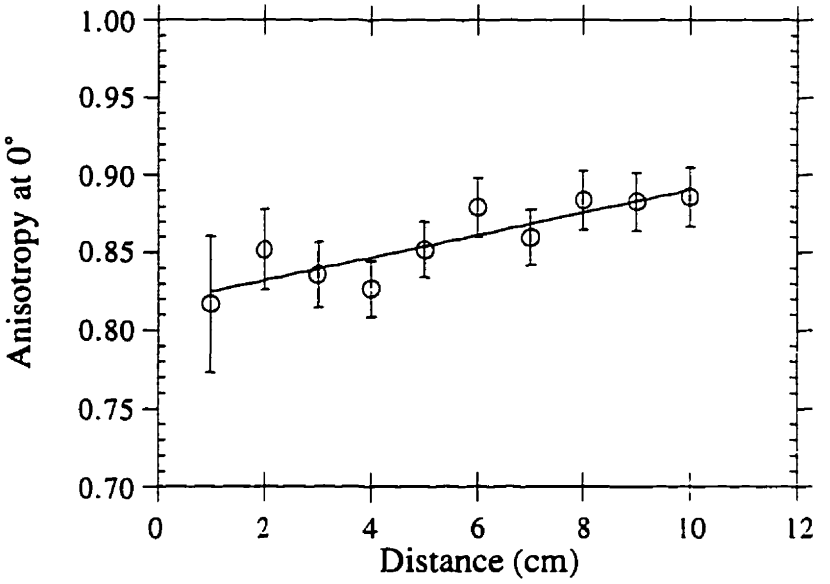

Figure 5.3 Variation of the anisotropy at the tip of the source as a function of the distance from the source.

Table 5.3 gives the ten anisotropy factors associated to the low dose-rate Ir-192 source. Using equation 3.20, we find that the average anisotropy factor, $\overline{\phi}_{an}$, is equal to 0.986.

Distance (cm)	Anisotropy factor, $\phi_{an}(r)$
1	0.986
2	0.986
3	0.989
4	0.986
5	0.986
6	0.986
7	0.991
8	0.985
9	0.979
10	0.983

Table 5.3 Anisotropy factor of the low dose-rate Ir-192 source as a function of the distance from the source.

5.1.2 Experimental Determination of the Radial Function, *g(r)*

As discussed in section 4.6.2, the radial function, *g(r)*, can be obtained using the dose measured at 90 degrees over the ten distances of interest.

Table 5.4 gives the measured dose rates normalised by calculation to a reference date.

Distance (cm)	Initial Dose Rate (cGy h^{-1}) (as if measured on a reference date)
1	20.7
2	5.36
3	2.37
4	1.36
5	0.851
6	0.598
7	0.424
8	0.325
9	0.250
10	0.201

Table 5.4 Initial dose rates calculated for a hypothetical reference date, for all ten distances.

Table 5.5 gives the ten values of the radial dose function, *g(r)*, for the low dose-rate Ir-192 source, using the procedure described in section 4.6.2.

Distance (cm)	Radial Dose Function, g(r)
1	1.000
2	1.014 ± 0.025
3	1.004 ± 0.031
4	1.011 ± 0.028
5	0.986 ± 0.027
6	0.990 ± 0.027
7	0.951 ± 0.026
8	0.946 ± 0.025
9	0.918 ± 0.025
10	0.904 ± 0.024

Table 5.5 The radial dose function, *g(r)*, for the low dose-rate Ir-192 source.

To obtain a smoother radial dose function, a third order polynomial fit was obtained using the raw data presented in table 5.5 taking care to anchor the polynomial representation of the radial dose function at unity at a distance of 1 cm (figure 5.4). The polynomial expression obtained is

$$g(r) = 0.9807 + 2.466\times10^{-2}r - 5.565\times10^{-3}r^2 + 2.321\times10^{-4}r^3 \qquad (5.1)$$

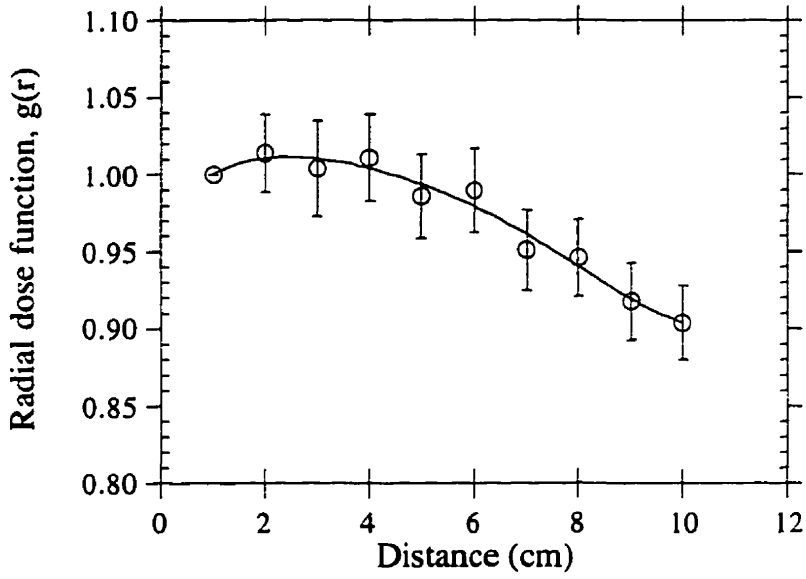

Figure 5.4 The radial dose function, *g(r)*, of the LDR Ir-192 source, with a solid line that represents the polynomial fit.

5.1.3 Experimental Determination of the Dose Rate Constant, Λ

A total of 24 dose rate measurements, performed on three different days over a period of ten weeks, lead to an estimate of $\Lambda = 1.110 \pm 2.9\%$ cGy h^{-1} U^{-1}.

5.2 Characterization of the High Dose-rate Ir-192 Source

5.2.1 Experimental Determination of the Anisotropy Function, $F(r,\theta)$

Similarly to the low dose-rate source, the first measurements of the anisotropy function were made at a distance of 10 cm (table 5.6 and figure 5.5).

Angles	Series #1	Series #2	Series #3	Series #4	Series #5	Average
0°	0.772	0.792	0.785	0.781	0.783	0.783 ± 0.016
10°	0.873	0.857	0.863	0.851	0.830	0.855 ± 0.018
20°	0.918	0.908	0.911	0.912	0.914	0.912 ± 0.019
30°	0.944	0.950	0.948	0.937	0.948	0.945 ± 0.020
40°	0.983	0.953	0.980	0.967	0.990	0.974 ± 0.020
50°	0.978	0.991	0.978	0.977	0.992	0.983 ± 0.021
60°	1.007	1.001	1.006	0.990	0.983	0.997 ± 0.021
70°	1.007	1.025	1.023	1.007	1.004	1.013 ± 0.021
80°	1.004	1.003	0.996	1.023	1.009	1.007 ± 0.021
90°	1.000	1.000	1.000	1.000	1.000	1.000
100°	1.011	1.001	0.977	0.997	1.000	0.997 ± 0.021
110°	1.000	1.001	0.996	0.992	0.987	0.995 ± 0.021
120°	0.992	0.981	0.973	0.981	0.964	0.978 ± 0.020
130°	0.960	0.975	0.955	0.954	0.972	0.963 ± 0.020
140°	0.949	0.928	0.931	0.910	0.946	0.933 ± 0.020
150°	0.919	0.916	0.901	0.881	0.904	0.904 ± 0.019
160°	0.875	0.864	0.847	0.844	0.863	0.859 ± 0.018
170°	0.774	0.787	0.777	0.752	0.788	0.776 ± 0.016

Table 5.6 Anisotropy function at a distance of 10 cm for five consecutive measurements.

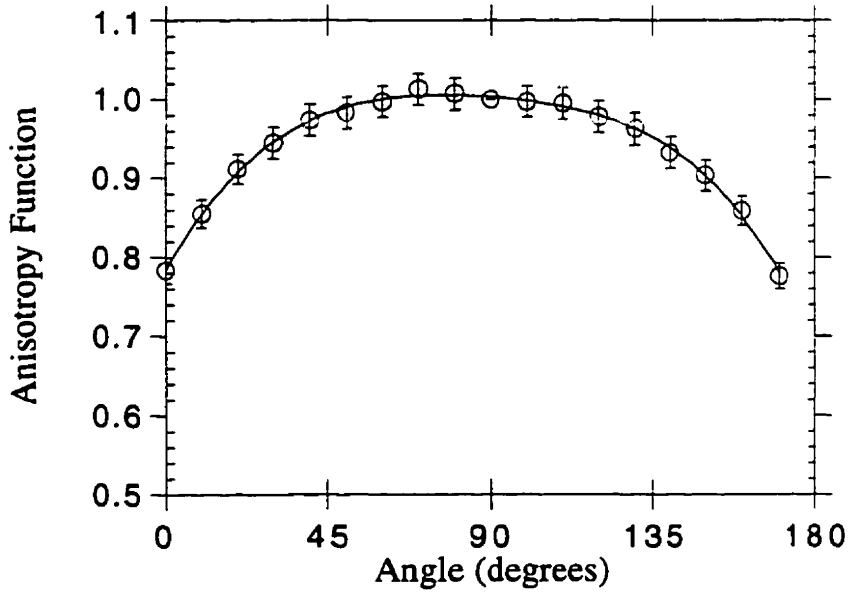

Figure 5.5 Anisotropy of the high dose-rate Ir-192 source at a distance of 10 cm, where the solid line is a polynomial best fit of the data points.

The anisotropy factor, ϕ_{an}, as determined with the procedure presented in section 3.7 is equal to 0.968.

The same procedure was used for the nine other distances of interest (table 5.7).

Angles	Distances									
	1 cm	2 cm	3cm	4 cm	5 cm	6 cm	7 cm	8 cm	9 cm	10 cm
0°	0.726 ±0.039	0.717 ±0.022	0.720 ±0.018	0.731 ±0.016	0.757 ±0.016	0.745 ±0.016	0.763 ±0.016	0.773 ±0.016	0.768 ±0.016	0.783 ±0.016
10°	0.797 ±0.042	0.810 ±0.025	0.818 ±0.020	0.823 ±0.018	0.837 ±0.018	0.832 ±0.017	0.834 ±0.017	0.841 ±0.018	0.837 ±0.018	0.855 ±0.018
20°	0.875 ±0.045	0.905 ±0.026	0.906 ±0.023	0.907 ±0.020	0.929 ±0.019	0.902 ±0.019	0.896 ±0.019	0.902 ±0.019	0.908 ±0.019	0.912 ±0.019
30°	0.923 ±0.043	0.951 ±0.028	0.950 ±0.024	0.959 ±0.021	0.967 ±0.020	0.949 ±0.020	0.944 ±0.020	0.939 ±0.020	0.933 ±0.020	0.945 ±0.020
40°	0.966 ±0.041	0.982 ±0.025	0.989 ±0.025	0.990 ±0.022	0.990 ±0.021	0.971 ±0.020	0.971 ±0.020	0.970 ±0.020	0.965 ±0.020	0.974 ±0.020
50°	0.981 ±0.036	1.003 ±0.025	1.001 ±0.025	1.005 ±0.022	1.012 ±0.021	0.987 ±0.021	0.984 ±0.021	0.984 ±0.021	0.983 ±0.021	0.983 ±0.021
60°	1.006 ±0.031	1.009 ±0.022	1.010 ±0.025	1.004 ±0.022	1.018 ±0.021	1.006 ±0.021	0.997 ±0.021	0.987 ±0.021	0.993 ±0.021	0.997 ±0.021
70°	0.984 ±0.025	1.011 ±0.021	1.001 ±0.025	1.012 ±0.022	1.030 ±0.022	1.000 ±0.021	1.008 ±0.021	1.010 ±0.021	0.999 ±0.021	1.013 ±0.021
80°	1.007 ±0.021	1.019 ±0.019	1.002 ±0.025	1.007 ±0.022	1.018 ±0.021	0.999 ±0.021	0.998 ±0.021	1.012 ±0.021	1.002 ±0.021	1.007 ±0.021
90°	*1.000*	*1.000*	*1.000*	*1.000*	*1.000*	*1.000*	*1.000*	*1.000*	*1.000*	*1.000*
100°	1.001 ±0.021	0.988 ±0.019	0.985 ±0.025	0.987 ±0.022	1.016 ±0.021	1.002 ±0.021	0.986 ±0.021	0.997 ±0.021	0.996 ±0.021	0.997 ±0.021
110°	0.984 ±0.025	0.965 ±0.020	0.962 ±0.024	0.984 ±0.022	0.997 ±0.021	0.997 ±0.021	0.994 ±0.021	0.991 ±0.021	0.991 ±0.021	0.995 ±0.021
120°	0.967 ±0.030	0.952 ±0.021	0.956 ±0.024	0.971 ±0.021	0.987 ±0.021	0.969 ±0.020	0.978 ±0.020	0.983 ±0.021	0.975 ±0.020	0.978 ±0.020
130°	0.948 ±0.035	0.926 ±0.023	0.927 ±0.023	0.942 ±0.021	0.971 ±0.020	0.965 ±0.020	0.965 ±0.020	0.964 ±0.020	0.961 ±0.020	0.963 ±0.020
140°	0.927 ±0.039	0.893 ±0.023	0.908 ±0.023	0.920 ±0.020	0.941 ±0.020	0.925 ±0.019	0.938 ±0.020	0.939 ±0.020	0.937 ±0.020	0.933 ±0.020
150°		0.856 ±0.025	0.860 ±0.021	0.870 ±0.019	0.912 ±0.019	0.908 ±0.019	0.911 ±0.019	0.918 ±0.019	0.906 ±0.019	0.904 ±0.019
160°		0.786 ±0.023	0.790 ±0.020	0.810 ±0.018	0.839 ±0.018	0.848 ±0.018	0.863 ±0.018	0.867 ±0.018	0.855 ±0.018	0.859 ±0.018
170°				0.709 ±0.016	0.739 ±0.015	0.750 ±0.016	0.781 ±0.016	0.787 ±0.016	0.779 ±0.016	0.776 ±0.016

Table 5.7 Anisotropy functions measured at distances from 1 to 10 cm, for the high dose-rate Iridium-192 source.

Figure 5.6 gives a plot of the 10 anisotropy functions presented in table 5.7. Each minor Y-axis division in figure 5.6 represents a value of 0.1.

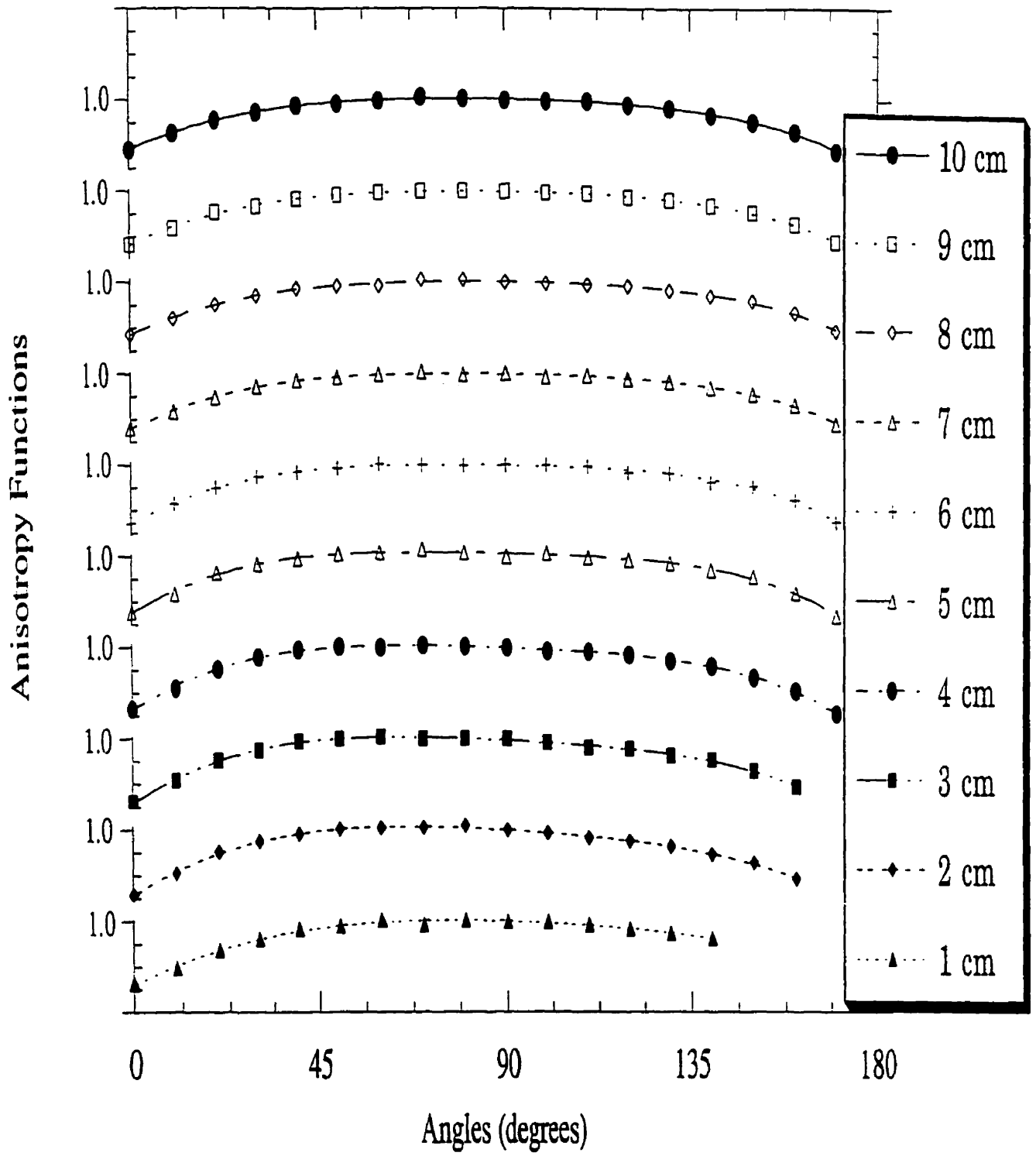

Figure 5.6 The complete anisotropy functions of the HDR Ir-192 source, with a modified ordinate axis. Each minor Y-axis division represents a value of 0.1.

The anisotropy of the HDR source decreases as the distance increases. Figure 5.7 shows a plot of the ten anisotropy values at the 0° angular position, where the solid line is a linear best fit of the experimental results. We see the effect of scattering on the variation of the anisotropy function with distance.

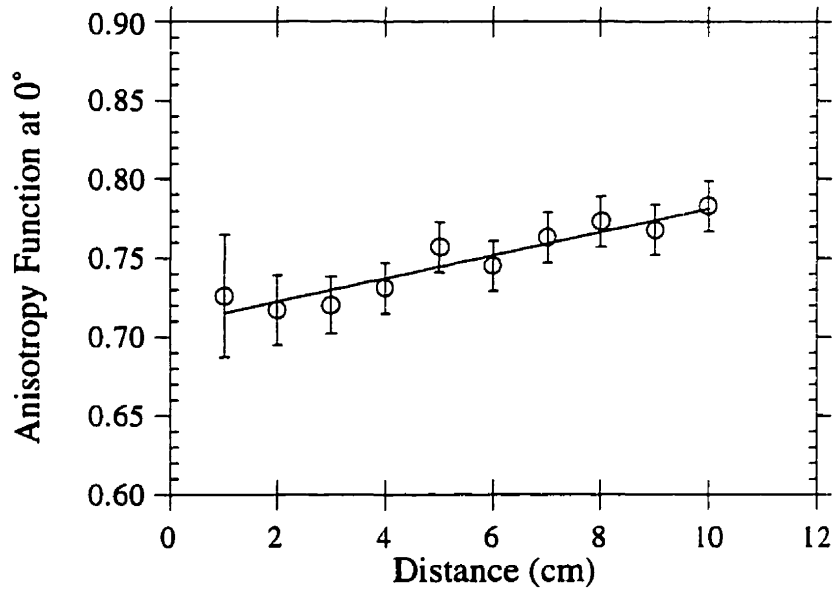

Figure 5.7 Anisotropy function at the tip of the HDR source as a function of the distance from the source.

Table 5.8 gives the ten anisotropy factors measured with the HDR Ir-192 source.

Using equation 3.20, the average anisotropy factor, $\overline{\phi}_{an}$, of the high dose-rate Ir-192 source is calculated to be 0.968.

Distance (cm)	Anisotropy factor, $\phi_{an}(r)$
1	0.971
2	0.960
3	0.959
4	0.964
5	0.980
6	0.967
7	0.967
8	0.969
9	0.966
10	0.969

Table 5.8 Anisotropy factor of the high dose-rate Ir-192 source as a function of distance from the source.

5.2.2 Experimental Determination of the Radial Function, $g(r)$

As discussed in section 4.6.2, the radial function, $g(r)$, can be obtained using the dose measured at 90 degrees over the ten distances of interest.

Table 5.9 gives the dose rates that would have been obtained at the 90° angular position, on a reference date (21 February 1997), for all 10 distances of interest.

Distance (cm)	Initial dose rate (cGy min^{-1}) (as if measured on a reference date)
1	529.1
2	136.6
3	60.30
4	33.91
5	21.46
6	15.25
7	10.73
8	8.18
9	6.39
10	5.10

Table 5.9 Initial dose rates calculated for a hypothetical reference date, for all ten distances.

Table 5.10 gives the ten values of the radial dose function, $g(r)$, for the high dose-rate Ir-192 source, using the procedure described in section 4.6.2.

Distance (cm)	Radial Dose Function, g(r)
1	1.000
2	1.017 ± 0.025
3	1.002 ± 0.031
4	0.994 ± 0.028
5	0.977 ± 0.026
6	0.993 ± 0.027
7	0.946 ± 0.026
8	0.937 ± 0.025
9	0.923 ± 0.025
10	0.900 ± 0.024

Table 5.10 The radial dose function, *g(r)*, for the high dose-rate Ir-192 source.

To obtain a smoother radial dose function, a third order polynomial fit was obtained using the raw data presented in table 5.10, taking care to anchor the polynomial representation of the radial dose function at unity at a distance of 1 cm (figure 5.8). The polynomial expression obtained is

$$g(r) = 0.9867 + 1.749 \times 10^{-2} r - 4.338 \times 10^{-3} r^2 + 1.737 \times 10^{-4} r^3 \qquad (5.4)$$

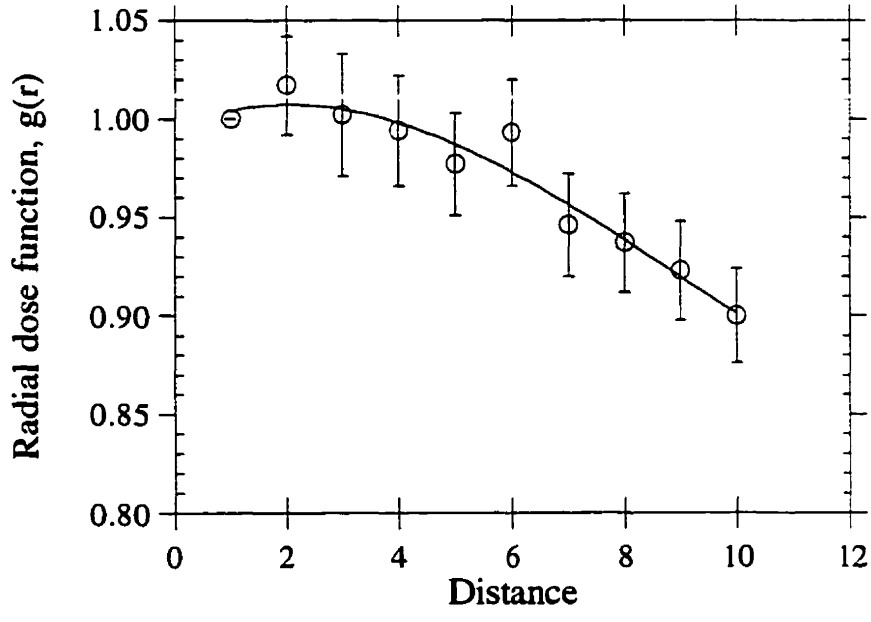

Figure 5.8 The radial dose function, *g(r)*, of the HDR Ir-192 source, with a solid line that represents the polynomial fit.

5.2.3 Experimental Determination of the Dose Rate Constant, Λ

A total of 24 dose rate measurements, performed on three different days over a period of ten weeks, lead to an estimate of $\Lambda = 1.134 \pm 2.9\%$.

6.0 DISCUSSION

6.1 Radial Dose Functions

Figure 6.1 compares the results obtained with the LDR Ir-192 source with the work of Meisberger (Meisberger *et al.* 1968) and two other experimental studies of low dose-rate Ir-192 sources (Thomason and Higgins 1989, Nath *et al.* 1990). The results of Meisberger are an average between measured values obtained with an anthracene scintillator with a Lucite light pipe to a photomultiplier and a set of calculated values. Nath *et al.* used LiF TLDs into a solid-water phantom to collect experimental results while Thomason and Higgins used LiF TLDs into a polystyrene phantom. In their analysis, Nath *et al.* applied the same depth dependent LiF sensitivity correction factors that we used in our study (Meigooni 1988b). On the other hand Thomason and Higgins concluded that there was no need to correct for an increasing LiF sensitivity with distance. Figure 6.1 illustrates that while the values of the radial dose function obtained by Thomason and Higgins stay close to unity even at a distance of 10 cm, our results agree well with the results obtained by the two other groups of investigators.

For the case of the HDR Ir-192 source, many recent studies, involving either experimental work or Monte Carlo simulations, have been published. Figure 6.2 compares the results obtained in our study with the same Meisberger factors discussed above, and with other published results (Podgorsak 1993a, Williamson and Li 1995). Podgorsak used a scintillation detector in a water tank. Williamson and Li used a Monte Carlo photon transport code to calculate the dose rate per unit air kerma strength in water medium. All results agree well.

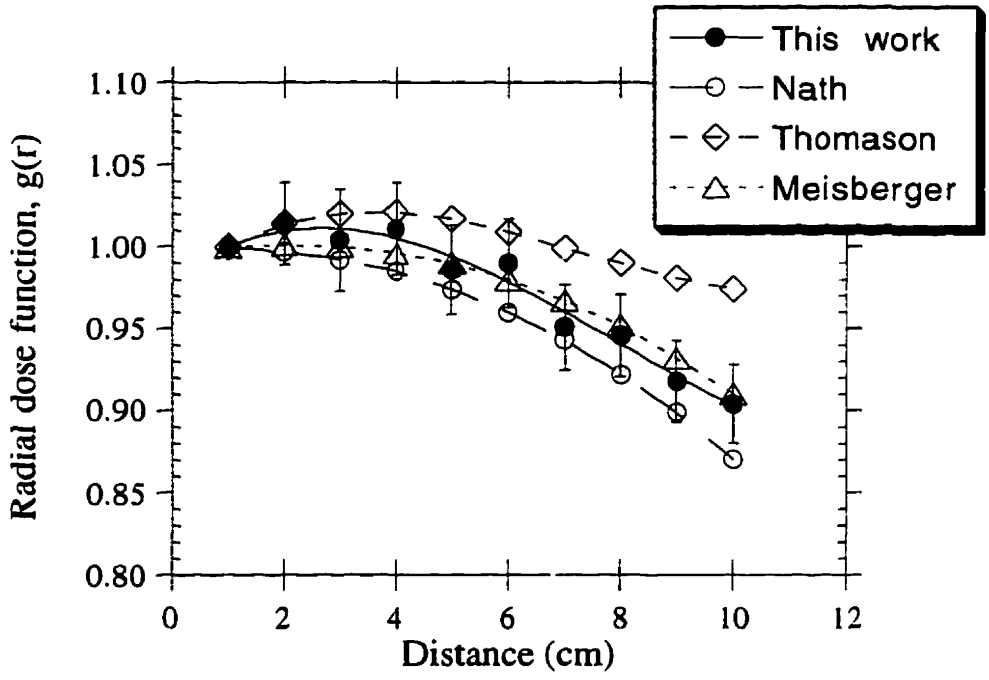

Figure 6.1 Comparison between the radial dose function, *g(r)*, of the LDR Ir-192 source measured within this project and similar published results.

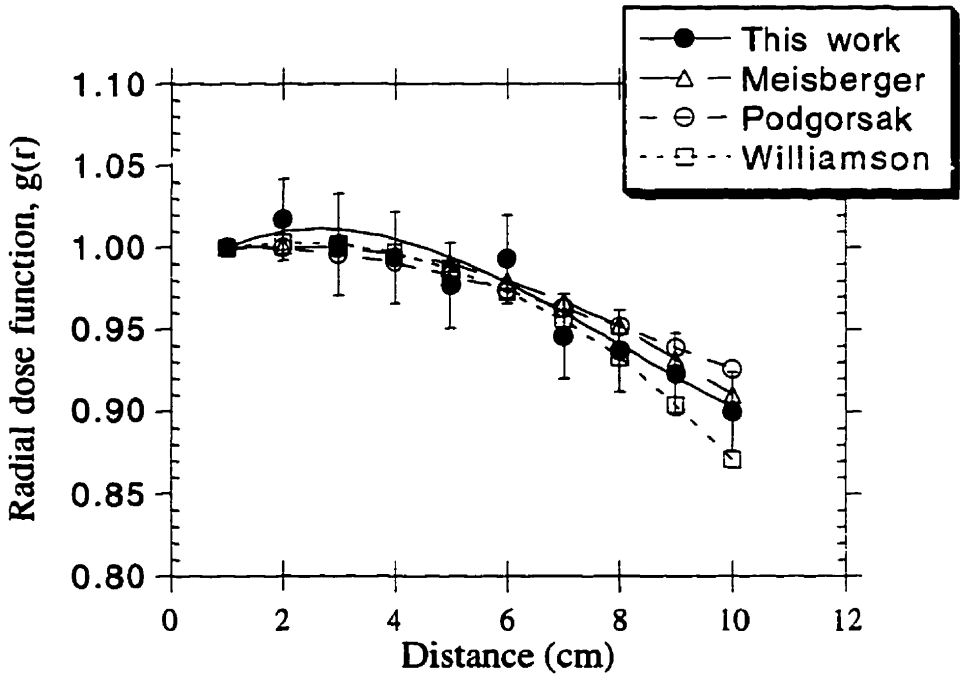

Figure 6.2 Comparison between the radial dose function, *g(r)*, of the HDR Ir-192 source measured within this project and similar published results.

6.2 Anisotropy functions

There are two main differences between the anisotropy functions with the LDR Ir-192 source and the ones with the HDR Ir-192 source and these differences are well illustrated in figure 6.3. The first major difference is the magnitude of the anisotropy of the sources at the angles furthest away from the transverse axis of the source. As illustrated in figure 6.3 for the case of $F(5\ cm, \theta)$, with the HDR source, the anisotropy function reduces to 0.76 at the tip of the source whereas the anisotropy of the LDR source equals 0.85 at the same angular position. This difference is caused by the larger source size and cladding associated with the HDR source that causes more attenuation. Another important difference between the anisotropy functions obtained with the different sources, clearly illustrated in figure 6.3, is that, while the anisotropy function of the LDR source is symmmetrical with respect to the transverse axis of the source, the anisotropy function of the HDR source is more peaked in the forward direction compared to symmetrical angular positions in the backward direction. This is explained by the presence of the cable attached to the HDR source which attenuates some radiation and, at the same time, produces less scattering that the missing water-equivalent medium.

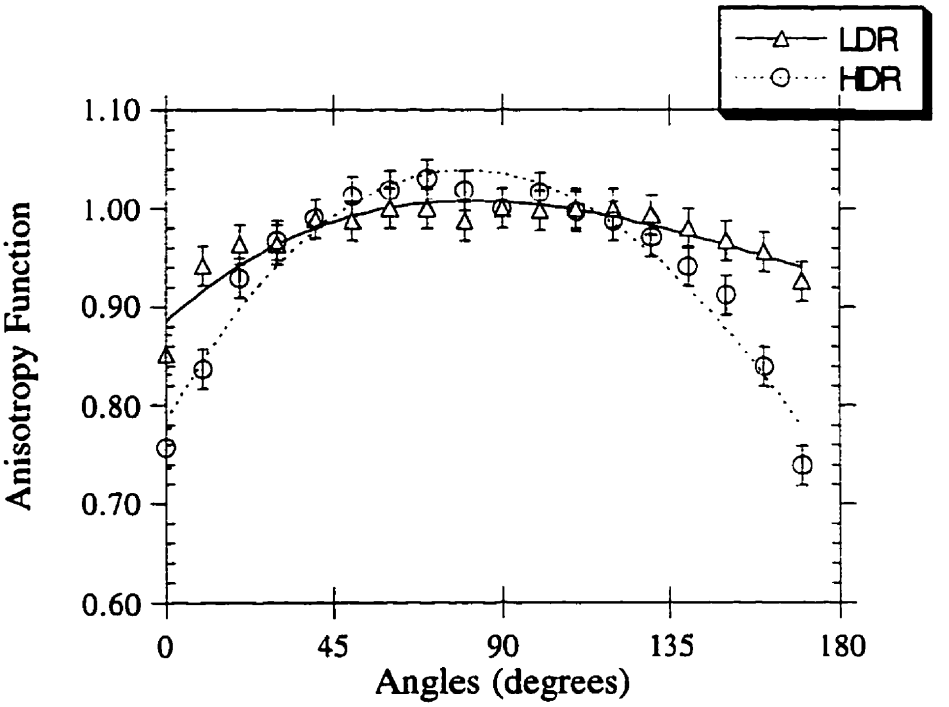

Figure 6.3 Comparison between the anisotropy functions obtained at a distance of 5 cm for both radioactive sources.

It is also interesting to compare the anisotropy functions obtained in this study with the HDR Ir-192 source to other experimental results or Monte Carlo simulations published in the literature concerning the same source. Table 6.1 compares for example the values of *F(5 cm, θ)* for many angles of interest and several authors. We see that even though all experimental results show a marked difference between *F(5 cm, 30°)* and *F(5 cm, 150°)*, both Monte Carlo simulations show equal values at these symmetrical angles. This is not because the Monte Carlo studies have neglected to model the source cable, as exemplified by their smaller values of *F(5 cm, 170°)* as compared to *F(5 cm, 10°)*. It is also surprising to see such a large difference in *F(5 cm, 0°)* between the two Monte Carlo simulations.

Anisotropy Function at 5 cm							
	Experimental Work					Monte Carlo Simulation	
Angle	This work	Mishra *et al.* 1997	Baltas *et al.* 1993	Zandona *et al.* 1995	Kirov *et al.* 1995	Williamson and Li 1995	Russel and Ahnesjö 1996
0°	0.76		0.77	0.74	0.72	0.70	0.80
10°	0.84	0.82	0.82	0.83		0.79	0.85
20°	0.93	0.90	0.89	0.90	0.86	0.87	0.89
30°	0.97	0.94	0.94	0.94		0.92	0.93
60°	1.02	0.98	0.99	1.01	0.98	0.99	0.99
90°	1.00	1.00	1.00	1.00	1.00	1.00	1.00
120°	0.99	0.98	0.96	0.98	0.96	0.99	0.99
150°	0.91	0.89	0.89			0.92	0.93
160°	0.84	0.83	0.85		0.86	0.86	0.89
170°	0.74	0.73	0.76			0.76	0.81

Table 6.1 Comparison of *F(5 cm, θ)* obtained by several authors with experimental work or Monte Carlo simulations.

This illustrates the need to perform complete anisotropy measurements for maximum accuracy while building anisotropy lookup tables for use by treatment planning computer programs.

6.3 Dose Rate Constants

Table 6.2 compares our estimate of the dose rate constant of the LDR Ir-192 source to other published results. We see that our results compare well to all the published results.

Author	Method	Λ (cGy h^{-1} U^{-1})
This work	TLD dosimetry	1.110 ± 2.9%
Meisberger 1968	Scintillation probe and photon transport calculation	1.12
Nath et al 1990	TLD dosimetry	1.09 ± 2.8%
Williamson 1991	Monte Carlo	1.110 ± 0.2%

Table 6.2 Dose rate constants obtained by various researchers for low dose-rate Ir-192 sources.

Table 6.3 compares our estimate of the dose rate constant of the HDR Ir-192 source to other results published in the literature. Only one other experimental determination of the dose rate constant for the microSelectron HDR Ir-192 source has been previously published (Kirov *et al.*, 1995). We see that our results compare well with the published values.

Author	Method	Λ (cGy h^{-1} U^{-1})
This work	TLD dosimetry	1.134 ± 2.9%
Kirov *et al.* 1995	Diode and TLD dosimetry	1.143 ± 5%
Williamson and Li 1995	Monte Carlo	1.115 ± 0.5%
Russel and Ahnesjö 1996	Monte Carlo	1.126 ± 1%

Table 6.3 Dose rate constants obtained by vavious researchers for high dose-rate Iridium-192 sources.

6.4 Clinical Application

This section discusses a vaginal boost treatment, where the use of the new TG 43 protocol offers advantages over the use of the point-source approximation protocol.

6.4.1 Use of the Point-source Approximation Protocol

A vaginal boost treatment is performed using a cylindrical mould inserted to touch the wall of the vagina. The applicator is a straight applicator. The dose is prescribed at 5 mm inside the vaginal wall.

With an Ir-192 HDR source, the isodose curves will not be circular since the source is characterized by a reduction of about 25 percent of the dose rate produced in the forward direction as compared to the dose rate produced at the same distance along the transverse axis of the source. The assumption of an isotropic dose distribution would therefore result in an underdosage at the tip of the source (table 6.5 below). A more accurate treatment planning has to account for the anisotropy of the radioactive source.

6.4.2 Use of the TG 43 Protocol

A more accurate treatment planning can be performed using the TG 43 protocol and a simple algorithm. Figure 6.4 illustrates that a treatment can be planned with two source positions and two points of prescription. The distance between the source position #2 and the points of prescription A and B is 2.25 cm and the distance between the source position #1 and the point of prescription A is 1.0 cm. A simple algorithm can be used to estimate the dwell time required at each position to produce a more uniform dose distribution at the points of prescription.

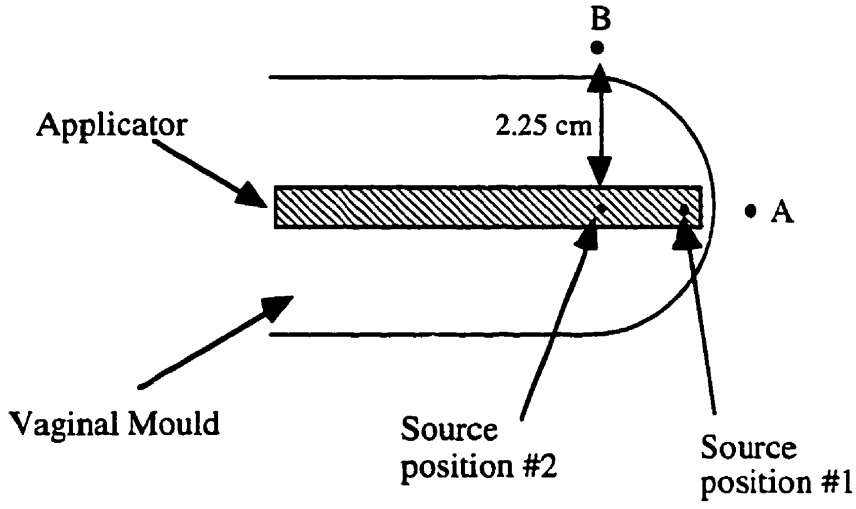

Figure 6.4 Schematic diagram of a vaginal boost treatment using two source positions to counterbalance the anisotropy of the radioactive source.

The following calculations illustrate how treatment dwell times can be determined.

A dose of 100 cGy is prescribed at the point B, on figure 6.4, and a dose of 90 cGy is prescribed at the position A, illustrated on the same figure. The dose prescribed at the point A was not set at exactly 100 cGy because we would then have obtained doses above 110 cGy at angular positions near 30° due to the anisotropy in the dose distribution produced by the source. Equation 3.1 can be rearranged as

$$\frac{\dot{D}}{S_k} = \Lambda \frac{G(r,\theta)}{G(1,\pi/2)} F(r,\theta) g(r) \qquad (6.1)$$

where $\dot{D}/S_k$ represents the dose rate per unit kerma strength of the radioactive source. At each point of interest, A and B in figure 6.4, we can determine the dose rate per unit air kerma strength produced by each of the two source positions. We then obtain two equations with two unknowns.

Table 6.4 presents the parameters required to construct the two dose-rate equations.

Data required for solving equation 6.1			
Variable	**With respect to source position...**	**Point A**	**Point B**
(r,θ)	#1	(1.0 cm, 0°)	(2.57 cm, 119°)
	#2	(2.25 cm, 0°)	(2.25 cm, 90°)
$F(r,\theta)$	#1	0.726	0.954
	#2	0.718	1.000
$g(r)$	#1	1.000	1.005
	#2	1.006	1.006
$G(r,\theta)/G(1\ cm,90°)$	#1	1.042	0.1529
	#2	0.2007	0.1991
$\dot{D}/S_k$ (cGy h^{-1} U^{-1})	#1	0.8579	0.1663
	#2	0.1644	0.2271

Table 6.4 Dosimetry factors used to find the proper source dwell times.

First, the coordinates (r,θ) of both points with respect to each source position are determined. We then use table 5.7, equation 5.4 and table 3.1B to respectively find the required values of the anisotropy function, the radial dose function and the geometry factor corresponding to the respective coordinates. By multiplication of the three respective terms and the dose rate constant, Λ, equal to 1.134 cGy h^{-1} U^{-1}, the dose rate produced by each source is calculated for each point of interest. These four numerical factors were used to form equations 6.2 and 6.3

$$90 \text{ cGy} / S_k = 0.8579 \text{ cGy h}^{-1} \text{ U}^{-1} \text{ X } T1 + 0.1644 \text{ cGy h}^{-1} \text{ U}^{-1} \text{ X } T2 \qquad (6.2)$$

$$100 \text{ cGy} / S_k = 0.1663 \text{ cGy h}^{-1} \text{ U}^{-1} \text{ X } T1 + 0.2271 \text{ cGy h}^{-1} \text{ U}^{-1} \text{ X } T2 \qquad (6.3)$$

Solving for T1, we find $T1$ = 23.86 h U S_k^{-1} or $T1$ = 85890 sec U S_k^{-1}; we also solve for T2, obtaining the result $T2$ = 1,522,000 sec U S_k^{-1}.

Using a source strength, S_k, of 14930 U, we obtain treatment times for $T1$ and $T2$ respectively of 5.8 sec and 102.0 sec. We see that the treatment time at the source position #1 is only a small fraction of the treatment time at the source position #2, and serves basically to build the small dose that is missing at the tip of the applicator due to the strong anisotropy of the source in that direction.

6.4.3 Measurements on a Modified Phantom

Two special inner pieces were built and fit into the puzzle phantom to measure the doses at points A and B produced by such dwell times, and also to measure the dose produced at many other points separated each by 7.5° along the semi-circle A-B. These measurements were required to verify the uniformity of the dose at a depth of 5 mm within the vaginal wall. Some extra measurements were also performed at distances of between 5 mm and 20 mm from the point of prescription at 90°, as illustrated in figure 6.5.

To provide for enough scattering material around each TLD rod, a first inner piece was machined with holes perforated at angular positions 0°, 15°, 30°, , and a second inner piece was machined with holes perforated at angular positions 7.5°, 22.5°, 37.5°,... Figure 6.6 is a photograph of the modified phantom.

The two dwell times obtained above were programmed into the microSelectron controller and a set of measurements was taken. Table 6.5 presents the results.

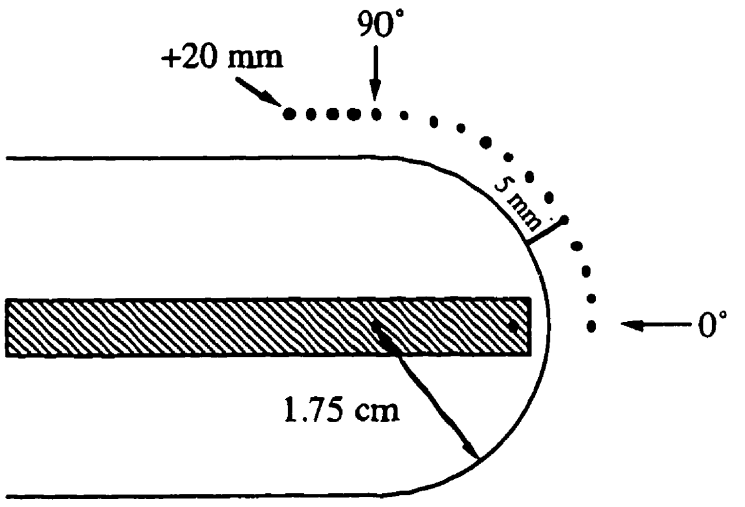

Figure 6.5 Positions where dose measurements were performed on the modified phantom.

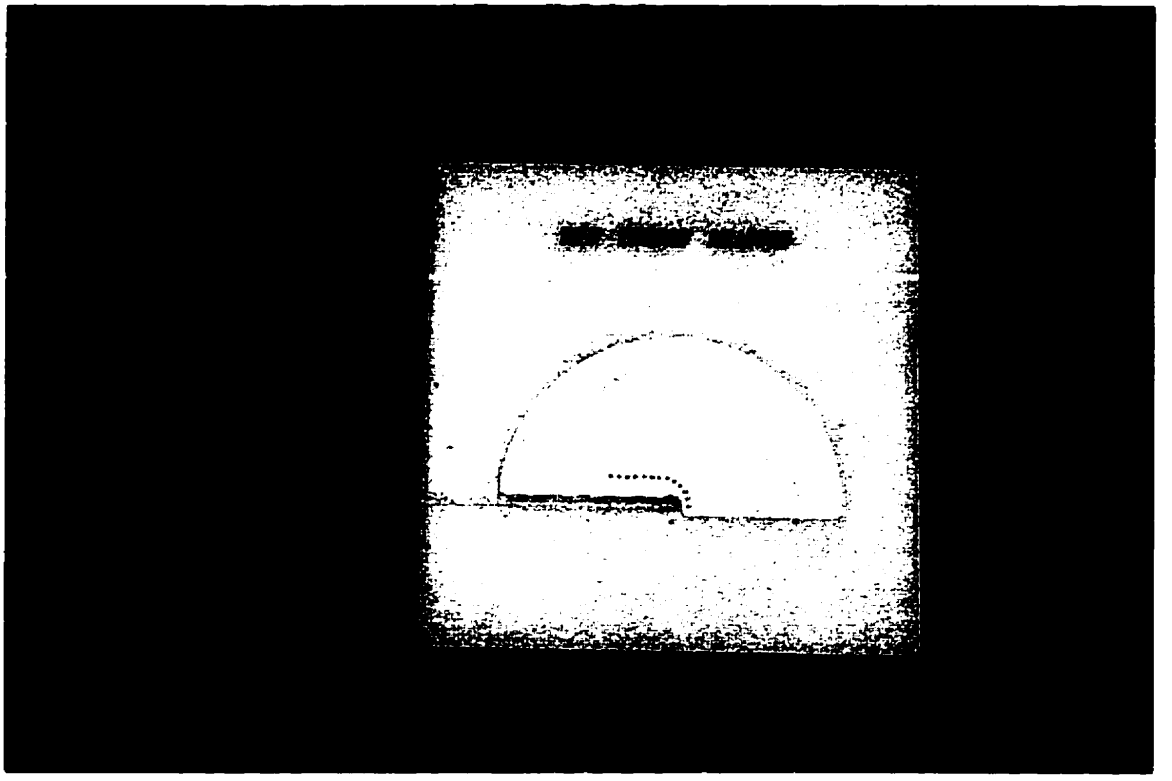

Figure 6.6 Photograph of the modified puzzle phantom.

TLD Position	Measured Dose (cGy)	Calculated dose for a single source position (cGy)
0°	98	73
7.5°	104	81
15°	107	88
22.5°	109	94
30°	110	97
37.5°	108	99
45°	107	101
52.5°	105	102
60°	108	103
67.5°	107	103
75°	103	103
82.5°	101	103
90°	102	102
+5 mm	93	
+10 mm	80	
+15 mm	66	
+20 mm	52	

Table 6.5 Doses measured with TLDs on a modified phantom to simulate a vaginal boost treatment as compared with calculated doses that would be obtained if the actual source was programmed only at source position #2 of figure 6.4.

The measurements reported in table 6.5 were performed to provide the medical personnel with an approximate estimate of the actual dose distribution produced by the source dwell times reported above, and are reproduced here to illustrate the use of the TG 43 protocol on a simple case. The measurements were taken only once, which means that there is some statistical uncertainty in these results due to the individual response of TLDs. Moreover no radiographs were taken to determine with precision the exact distance between the source and the TLD rods. A uncertainty of approximately 0.5 mm may be assumed for any positioning error. The TLD sensitivity factor that varies between approximately 1.015 and 1.075 for source-to-TLD distances of 1 to 10 cm was set to 1.02 for all measurements because most of the integrated dose was produced by the source at position #2 and the distance between this source position and the points of measurements is equal to 2.25 cm. It was not judged necessary to determine for each of the 17 points of measurements the exact distance from the two source positions and the fraction of the dose produced by each source position to obtained a more accurate TLD sensitivity correction factor.

In addition, table 6.5 gives the dose that would be obtained if the actual HDR Ir-192 source was used only at the source position #2. These values were obtained by interpolation form table 5.7 and normalising at 102 cGy the dose given on the transverse axis of the source.

As seen in table 6.5, the dose distribution at 5 mm inside the vaginal wall, as measured with the modified phantom, is more uniform than the dose that would be obtained by using the actual source at only one position, since the treatment using two source positions is able to correct for the forward underdosage we would have seen if the treatment procedure had been based on a single source position. We see that for points along the semi-circle between points A and B, the measured dose vary between approximately 96% and 108% of the dose measured at the point of prescription B, which is acceptable considering the experimental uncertainties mentioned above.

This example proves that a simple algorithm can be used to correct for the intrinsic anisotropy of an HDR Ir-192 source.

7.0 CONCLUSION

The aim of this research project was to build a complete two-dimensional dose distribution data bank for both a low dose-rate and a high dose-rate Iridium-192 brachytherapy source. To obtain these data banks, a suitable water-equivalent phantom was designed and built. Thermoluminescent detectors were selected for the measurements because of their precise positioning and their very good spatial resolution and also because of their ability to integrate the dose during the measurement process.

Because the response of a thermoluminescent detector can vary from a given measurement to the next one, each measurement was performed five times to reduce the statistical uncertainty of an individual result. While the use of a control TLD removed the error due to TLD positioning in the transverse axis of the source for the 1-cm and 2-cm distances, there were some uncertainty in the TLD positioning in the longitudinal axis of the source, which produced potential error margins due to positioning only, of approximately ± 5% in the evaluation of the anisotropy function at a distance of 1 cm. For all distances and angles where experimental data were obtained, the overall uncertainty in determination of dose rate around the sources, using the TG 43 protocol, does not exceed 10%.

These data banks served to determine the dosimetry functions defined by the new TG 43 protocol. Clinical medical physicists have been asking recently for such results because the accuracy of dose delivery in brachytherapy is directly proportional to the accuracy with which the radiation parameters of radioactive souces are known.

The dose distribution for an illustrative clinical case, a vaginal boost, was also calculated using a simple algorithm and the data bank obtained within this research project. Measurements were also performed on a special phantom to assess the accuracy of this simple algorithm.

The use of the point-source approximation in many dosimetry protocols currently in use can lead to errors in dose delivery. For some treatments, where the dose is mainly delivered by radiation emitted within 45° of the transverse direction of the sources, the TG 43 protocol does not give results significantly different than results obtained with the current point-source approximation protocol. Results presented above have shown that an Ir-192 source does not suffer much from anisotropy in this angular coverage. However there are clinical situations, like vaginal boosts, where the use the point-source

approximation protocol may result in an overestimation of the dose to clinically relevant points. Results presented in this work have demonstrated that the use of the point-source approximation protocol can overestimate dose by factors that vary between 22 and 28 percent at the tip of a vaginal cylinder (0° angular position) for distances that respectively vary between 10 cm and 1 cm, with an HDR Ir-192 source.

The systematic use of the air kerma strength instead of the apparent activity to characterize the source can eliminate potential errors. It is presently for a clinical physicist to use a different value for the air kerma rate constant than the value used by the manufacturer to determine the apparent activity of the source. The calculated dose may therefore be wrong. Medical physicists should be aware of this potential source of errors and comply with the recommendations of the TG 43 in using only the air kerma strength as the sole input parameter to describe the strength of a brachytherapy source. This change of habit can be initiated without a complete conversion to the TG 43 protocol, since the air kerma strength can very well characterize the strength of a radioactive source in a point-source approximation protocol.

Simple modifications to a point-source dosimetry protocol can also lead to a slightly more accurate representation of the inverse square law by the use of the geometry factor, and some source anisotropy can be accounted for by using the anisotropy factor in the point-source dosimetry protocol. The use of the anisotropy factor would not produce a satisfactory result for a vaginal boost treatment, since the anisotropy at the tip of a high dose-rate source is very large.

Some other authors have found the dosimetry functions of Ir-192 sources and have published experimental results (Thomason and Higgins 1989, Baltas *et al.* 1993, Nath *et al.* 1993, Muller-Runkel and Cho 1994, Kirov *et al.* 1995). However, the published results are generally restricted to a few distances or angular positions that cannot be used to produce a complete two-dimensional dose distribution matrix with any degree of accuracy. Some authors have also published dose distribution tables obtained by Monte Carlo computerized simulations (Thomason *et al.* 1991, Sakelliou *et al.* 1992, Williamson and Li 1995, Russel and Ahnesjö 1996). Some of these authors have tried to compare the Monte Carlo simulations to the limited available experimental results. The idea is that if the simulations and the experimental results give the same values at some positions relative to the source, the authors then assume that the results obtained with Monte Carlo simulations at all angles and distances (although never measured) are reliable and can be used for

treatment. However, when we compared results obtained by Monte Carlo simulations by various authors, some significant differences were noted and it was difficult to determine which one of the tables was more accurate at representing the source. There might exist small differences in the geometric configuration of sources and applicators between the various simulations. The results of this study helped to remove this uncertainty by providing an extensive set of experimental dosimetry data for the low dose-rate and high dose-rate brachytherapy Ir-192 sources, filling a gap in the current literature.

Some new planning software offer users the possibility to input the TG 43 dosimetry parameters associated with brachytherapy sources used in their clinic. For such cases, the results of this study can be systematically used. For clinical medical physicists who do not have access to these modern software, the anisotropy results obtained in this study can be used with the simple algorithm discussed in section 6.4 to improve treatments by using two or more source positions to correct for the anisotropy of Ir-192 sources.

This study has demonstrated that thermoluminescent dosimetry is a reliable dosimetry technique. However, thermoluminescent dosimetry is extremely time consuming and other detectors will have to be developed if clinicians need to measure rapidly and accurately the dose at a large number of points around a brachytherapy source in a scattering medium.

8.0 REFERENCES

Baltas D, Kramer R and Löffler E 1993 Measurements of the anisotropy of the new Ir-192 source for the microSelectron-HDR *Activity Special Report* **3** 2-8

Bastin K T, Podgorsak M B and Thomadsen B R 1993 The transit dose component of high dose rate brachytherapy: direct measurements and clinical implications *Int. J. Radiation Oncology Biol. Phys.* **26** 695-702

Bevington P R and Robinson D K 1992 *Data Reduction and Error Analysis for the Physical Sciences 2nd edition* (New York: McGraw Hill)

Booth L F, Johnson T L and Attix F H 1972 Lithium fluoride glow-peak growth due to annealing *Health Phys* **23** 137-141

Cameron J R, Zimmerman D, Bush R, Bland R and Grant R M 1964 Thermoluminescence radiation dosimetry utilizing LiF *Health Phys.* **10** 25

Comité Français pour la Mesure des Rayonnements Ionisants (CFMRI) 1982 *Recommandations pour la détermination des doses absorbées en curiethérapie, Rapport no. 1* (Paris: Bureau National de Métrologie)

Dhar A, DeWerd L A. and Stroebe T G Effects of annealing and cooling progress on thermoluminescence of LiF (TLD-100) 1973 *Health Phys* **25** 427-433

Ezzell G A 1993 Evaluation of new re-entrant ionization chambers for high dose rate brachytherapy calibrations *Endocur. Hypertherm. Oncol.* **9** 233-237

Gillin M T, Lopez F, Kline R W, Grimm D F and Niroomand-Rad A 1988 Comparison of measured and calculated dose distributions around an Iridium-192 wire *Med. Phys.* **15** 915-918

Glasgow G P and Dillman L T 1979 Specific γ-ray constant and exposure rate constant of Ir-192 *Med. Phys.* **6** 49-52

Goetsch S J, Attix F H, Pearson D W and Thomadsen B R 1991 Calibration of Ir-192 high-dose-rate afterloading systems *Med. Phys.* **18** 462-467

Houdek P V, Schwade J G, Wu X, Pisciotta V, Fiedler J A, Serago C F, Markoe A M, Abitbol A A, Lewin A A, Braunschweiger P G and Sklar M D 1992 Dose determination in high dose-rate brachytherapy *Int. J. Radiation Oncology Biol. Phys.* **24** 795-801

Horowitz Y S 1981 The theoretical and microdosimetric basis of thermoluminescence and applications to dosimetry *Phys. Med. Biol.* **26** 765-824

International Commission on Radiation Units and Measurements (ICRU) 1976 *Determination of Absorbed Dose in a Patient Irradiated by Beams of X or Gamma Rays in Radiotherapy Procedures" Report No. 24* (Washington, DC: ICRU)

Interstitial Collaborative Working Groups (ICWG) 1990 *Interstitial Brachytherapy: Physical, Biological, and Clinical Considerations* ed L L Anderson, R Nath and K A Weaver (New York: Raven)

Johns H E and Cunningham J R 1983 *The Physics of Radiology 4th edition* (Springfield: CC Thomas)

Kirov A S, Williamson J F, Meigooni A S and Zhu Y 1995 TLD, diode and Monte Carlo dosimetry of an Ir-192 source for high dose-rate brachytherapy *Phys. Med. Biol.* **40** 2015-2036

Kornelson R O and Young M E J 1981 Brachytherapy build-up factors *Br. J. Radiol.* **54** 136

Kron T, Metcalfe P and Wong T 1993 Thermoluminescence dosimetry of therapeutic X-rays with LiF ribbons and rods *Phys. Med. Biol.* **38** 833-845

Lederer D M and Shirley V eds. 1978 *Table of Isotopes 7th edition* (New York: John Wiley & Sons)

Luxton G, Astrahan M A, Findley D O and Petrovich Z 1990 Measurement of dose rate from exposure-calibrated I-125 seeds *Int. J. Radiation Oncology Biol. Phys.* **18** 1199-1207

Meigooni A S, Meli J A and Nath R 1988a A comparison of solid phantoms with water for dosimetry of I-125 brachytherapy sources *Med. Phys.* **15** 695-701

Meigooni A S, Meli J A and Nath R 1988b Influence of the variation of energy spectra with depth in the dosimetry of Ir-192 LiF TLD *Phys. Med. Biol.* **33** 1159-1170

Meigooni A S, Mishra V, Panth H and Williamson J 1995 Instrumentation and dosimeter-size artifacts in quantitative thermoluminescence dosimetry of Low-dose fields *Med. Phys.* **22** 555-561

Meisberger L L, Keller R and Shalek R J 1968 The effective attenuation in water of the gamma rays of ^{198}Au, ^{192}Ir, ^{137}Cs, ^{226}Ra, and ^{60}Co *Radiology* **90** 953-957

Meli J A, Meigooni A S and Nath R 1988 On the choice of phantom material for dosimetry of ^{192}Ir sources *Int. J. Radiat. Onco.* **14** 587-594

Mishra V, Waterman F M and Suntharalingam N 1997 Anisotropy of an Iridium-192 high dose rate source measured with a miniature ionization chamber *Med. Phys.* **24** 751-755

Muench P J, Meigooni A S, Nath R and McLaughlin W L 1991 Photon energy dependence of the sensitivity of radiochromic film and comparison with silver halide film and LiF TLDs used for brachytherapy dosimetry *Med. Phys.* **18** 769-775

Muller-Runkel R and Cho S H 1994 Anisotropy measurements of high-dose rate Ir-192 source in air and in polystyrene *Med. Phys.* **21** 1131-1134

Nath R, Meigooni A S and Meli J A 1990 Dosimetry on the transverse axis of ^{125}I and ^{192}Ir interstitial brachytherapy sources *Med. Phys.* **17** 1032-1040

Nath R 1993 New directions in radionuclide sources for brachytherapy *Seminars in Radiation Oncology* **3** 278-289

Nath R, Meigooni A S, Muench P and Melillo A 1993 Anisotropy functions for Pd-103, I-125 and Ir-192 interstitial brachytherapy sources *Med. Phys.* **20** 1465-1473

Nath R, Anderson L L, Luxton G, Weaver K A, Williamson J F and Meigooni A S 1995 Dosimetry of Interstitial Brachytherapy Sources: Recommandations of the AAPM Radiation Therapy Committee Task Group No. 43 *Med. Phys.* **22** 209-234

Paterson R and Parker A M 1934 A dosage system for gamma ray therapy *Br. J. Radiol.* **7** 592-612

Perera H, Williamson J F, Monthofer S P, Binns W R, Klarman J, Fuller G L and Wong J W 1992 Rapid two-dimensional dose measurement in brachytherapy using plastic scintillator sheet: linearity, signal-to-noise ratio and energy response characteristics *Int. J. Radiat. Oncol. Biol. Phys.* **23** 1059-1069

Perera H, Williamson J F, Li Z, Mishra V and Meigooni A S Dosimetric characteristics, air-kerma strength calibration, and verification of Monte Carlo simulation for a new Yb-169 brachytherapy source 1994 *Int. J. Radiat. Oncol. Biol. Phys.* **28** 953-970

Pla C 1989 Fast intracavitary and interstitial treatment planning in *Brachytherapy 2* (Leersum, Holland: Nucletron) 109-120

Podgorsak M B 1993a *Radiation parameters of high dose rate Iridium-192 sources Ph. D. thesis* (Madison: University of Wisconsin)

Podgorsak M B, DeWerd L A and Paliwal B R 1993b The half-life of high dose rate Ir-192 sources *Med. Phys.* **20** 1257-1259

Quimby E H 1944 Dosage tables for linear radium sources *Radiology* **43** 572-577

Russell K R and Ahnesjö A 1996 Dose calculation in brachytherapy for an Ir-192 source using a primary and scatter dose separation technique *Phys. Med. Biol.* **41** 1007-1024

Sakelliou L, Sakellariou K, Sarigiannis K, Angelopoulos A, Perris A and Zarris G 1992 Dose rate distributions around Co-60, Cs-137, Au-198, Ir-192, Am-241, I-125 brachytherapy sources and the nuclide Tc-99m *Phys. Med. Biol.* **37** 1859-1872

Serago C F, Houdek P V, Pisciotta V, Schwade J G, Abitbol A A, Lewin A A, Poole D O and Marcial-Vega V 1991 Scattering effects on the dosimetry of Ir-192 *Med. Phys.* **18** 1266-1270

Thomason C and Higgins P 1989 Radial dose distribution of Ir-192 and Cs-137 sources *Med. Phys.* **16** 254-257

Thomason C, Mackie T R, Lindstrom M J and Higgins P D 1991 The dose distribution surrounding ^{192}Ir and ^{137}Cs seed sources *Phys. Med. Biol.* **36** 475-493

Weaver K A, Smith V, Huang D, Barnett C, Schell M C and Ling C 1989 Dose parameters of ^{125}I and ^{192}Ir seed sources *Med. Phys.* **16** 636-643

Williamson J F 1991 Comparison of measured and calculated dose rates in water near I-125 and Ir-192 seeds *Med. Phys.* **18** 776-786

Williamson J F, Perera H, Li Z and Lutz W R 1993 Comparison of calculated and measured heterogeneity correction factors for I-125, Cs-137 and Ir-192 brachytherapy sources near localized heterogeneities *Med. Phys.* **20** 209-221

Williamson J F and Li Z 1995 Monte Carlo aided dosimetry of the microselectron pulsed and high dose-rate Ir-192 sources *Med. Phys.* **22** 809-819

Zandona R, Riccardi L, Cauzzo C, Simonato F, Merlo C, Bolla E and Fabrris R 1995 Anisotropy of a microSelectron HDR Iridium-192 source", *Activity report No. 7* 39-42

IMAGE EVALUATION
TEST TARGET (QA-3)

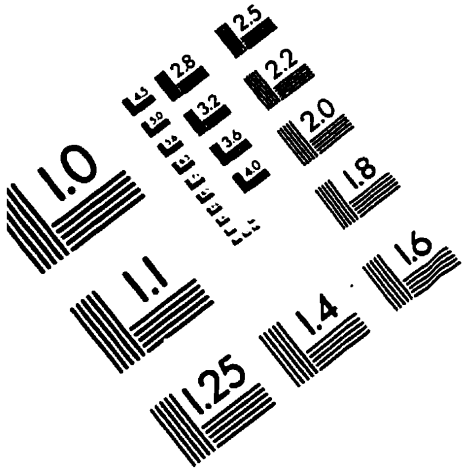

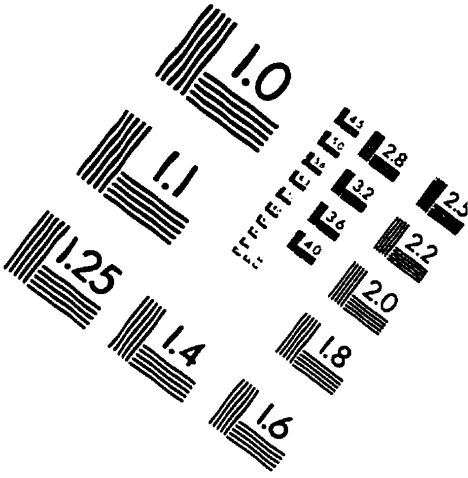

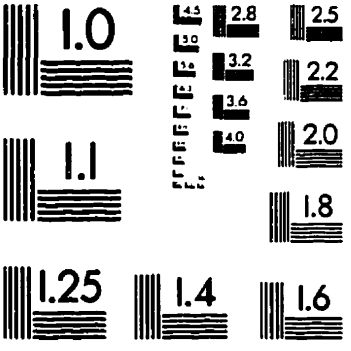

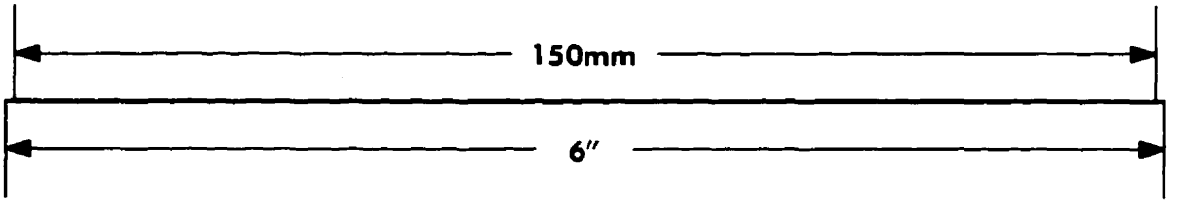

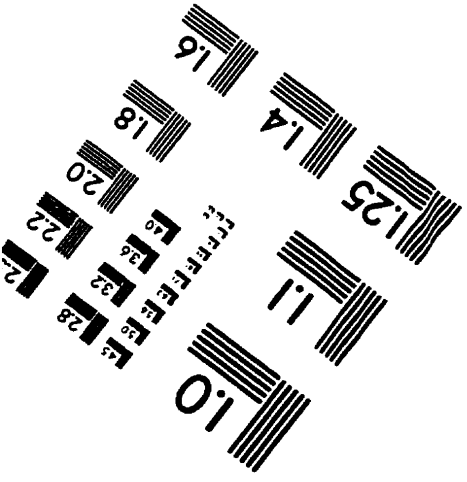

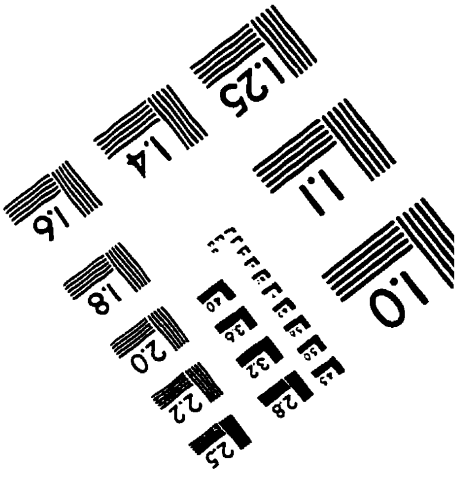

APPLIED IMAGE, Inc
1653 East Main Street
Rochester, NY 14609 USA
Phone: 716/482-0300
Fax: 716/288-5989